

# Daily electrical activity in the master circadian clock of a diurnal mammal

Beatrix Bano-Otalora<sup>1,2,†</sup>, Matthew J. Moye<sup>3,4,†</sup>, Timothy M. Brown<sup>1,5</sup>,

Robert J. Lucas<sup>1,2,\*</sup>, Casey O. Diekman<sup>3,6,\*</sup>, Mino D. C. Belle<sup>7,\*</sup>

<sup>1</sup>*Centre for Biological Timing, Faculty of Biology Medicine & Health, University of Manchester, Manchester, UK.*

<sup>2</sup>*Division of Neuroscience and Experimental Psychology, Faculty of Biology Medicine and Health, University of Manchester, Manchester, UK.*

<sup>3</sup>*Department of Mathematical Sciences, New Jersey Institute of Technology, Newark, NJ, USA.*

<sup>4</sup>*Department of Quantitative Pharmacology & Pharmacometrics (QP2) at Merck & Co. Inc., Kenilworth, New Jersey, USA.*

<sup>5</sup>*Division of Diabetes, Endocrinology and Gastroenterology, Faculty of Biology Medicine and Health, University of Manchester, Manchester, UK.*

<sup>6</sup>*EPSRC Centre for Predictive Modelling in Healthcare, Living Systems Institute, University of Exeter, Exeter, UK.*

<sup>7</sup>*Institute of Biomedical and Clinical Sciences, University of Exeter Medical School, University of Exeter, Exeter, UK.*

<sup>†</sup>Authors contributed equally to this work.

\*Corresponding Authors: [m.d.c.belle@exeter.ac.uk](mailto:m.d.c.belle@exeter.ac.uk), [casey.o.diekman@njit.edu](mailto:casey.o.diekman@njit.edu) and [robert.lucas@manchester.ac.uk](mailto:robert.lucas@manchester.ac.uk)

## Abstract

Daily or circadian rhythms in mammals are orchestrated by a master circadian clock within the hypothalamic suprachiasmatic nuclei (SCN). Here, cell-autonomous oscillations in gene expression, intrinsic membrane properties, and synaptic communication shape the electrical landscape of the SCN across the circadian day, rendering SCN neurons overtly more active during the day than at night. This well-accepted hallmark bioelectrical feature of the SCN has overwhelmingly emerged from studies performed on a small number of nocturnal rodent species. Therefore, for the first time, we investigate the spontaneous and evoked electrical activity of SCN neurons in a diurnal mammal. To this end, we measured the electrical activity of individual SCN neurons during the day and at night in brain slices prepared from the diurnal murid rodent *Rhabdomys pumilio* and then developed cutting-edge data assimilation and mathematical modelling approaches to uncover the underlying ionic mechanisms. We find that *R. pumilio* SCN neurons were more excited in the day than at night, recapitulating the prototypical pattern of SCN neuronal activity previously observed in nocturnal rodents. By contrast, the evoked activity of *R. pumilio* neurons included a prominent suppressive response that is not present in the SCN of nocturnal rodents. Our computational modelling

approaches reveal transient subthreshold A-type potassium channels as the primary determinant of the suppressive response and highlight a key role for this ionic mechanism in tuning excitability of clock neurons and optimising SCN function to accommodate *R. pumilio*'s diurnal niche.

Keywords: diurnality, circadian rhythms, suprachiasmatic nucleus, electrical activity, mathematical modelling, data assimilation

## INTRODUCTION

The mammalian master circadian clock is localized within the hypothalamic suprachiasmatic nucleus (SCN), where nearly 20,000 neurons synchronize their daily activity with the light-dark cycle to orchestrate circadian rhythms in physiology and behaviour (Reppert & Weaver, 2002). SCN neurons are electrically and chemically heterogeneous. Most, if not all, SCN neurons contain an internal molecular clock that operates on a transcription-translation feedback loop (TTFL) (Ko & Takahashi, 2006). Activity of the TTFL drives circadian rhythms in electrical activity, with SCN neurons notably more active during the day (up-state) than at night (down-state). This excitability landscape within the SCN is reinforced by the appropriate synaptic integration of extrinsic signals, which includes photic information from the retina and behavioural feedback reflecting arousal state (Belle & Diekman, 2018).

Our current understanding of SCN neurophysiology comes overwhelmingly from electrophysiological recordings on a small number of nocturnal rodent species (mice, rats and hamsters) (Colwell, 2011; Belle & Diekman, 2018; Harvey *et al.*, 2020). A handful of studies have confirmed that the daytime peak in spontaneous activity (as reflected in extracellular electrical activity or deoxyglucose uptake) is retained in the SCN of diurnal species (Sato & Kawamura, 1984; Schwartz, 1991; Ruby & Heller, 1996). However, there has been no whole-cell recording of SCN neurons from a diurnal species, and the question of how, or if, SCN neurophysiology is altered to accommodate a diurnal niche remains unanswered. *Rhabdomys pumilio* (the four striped mouse) represents an excellent opportunity to address this question. This species is strongly diurnal (Dewsbury & Dawson, 1979; Schumann *et al.*, 2005; Bano-Otalora *et al.*, 2020) and is a murid rodent, facilitating comparison with established findings from closely related nocturnal species (mice and rats).

We adopted a parallel approach of experimental recording and advanced computational modelling to understand the *R. pumilio* SCN. First, we address the lack of data on single-cell physiology in diurnal SCN by using whole-cell recordings to describe spontaneous electrical states and their daily variation. We then determined the evoked membrane properties of these diurnal SCN neurons by recording their responses to inputs. We then turned to cutting-edge data assimilation and modelling approaches to gain insight into the cellular and ionic mechanisms underlying passive and evoked electrical states. Our results revealed similarities in SCN neurophysiology between the *R. pumilio* and other rodent species, but also exposed fundamental differences which may serve to accommodate SCN functioning to a diurnal niche.

## RESULTS

### SCN neuropeptidergic organization in the diurnal *Rhabdomys pumilio*.

Prior to assaying single-cell electrical properties in the *R. pumilio* SCN, we first described the anatomical and neuropeptidergic organization of the SCN in this species. This provided us with a practical guide to ensure only neurons within the SCN were targeted for electrophysiology since no brain atlas yet exists for this species. To this end, we performed immunofluorescence labelling for nuclear DNA with DAPI, vasoactive intestinal polypeptide (VIP), arginine vasopressin (AVP), and gastrin-releasing peptide (GRP) (Fig.1).

The gross neuroanatomy of the *R. pumilio* SCN across the rostro-caudal axis is broadly similar to other rodent species (Smale & Boverhof, 1999; Abrahamson & Moore, 2001)

(Fig.1A). Immunofluorescence labelling for the main neuropeptides showed that the *R. pumilio* SCN contains VIP, AVP, and GRP, and importantly, the neuroanatomical localization of these neuropeptides was broadly similar to the distribution found in other rodent species (Smale & Boverhof, 1999; Abrahamson & Moore, 2001), AVP-positive cell bodies were mainly localized in the dorsomedial aspect (sometimes termed “shell” (Fig.1B)), while VIP-positive somas were localized throughout the ventral region or “core”, with VIP immunoreactive axonal processes extended into the dorsal SCN (Fig.1C). By contrast, GRP-positive neurons were localized in the central SCN (Fig.1D).

### **Diurnal changes in the spontaneous electrical activity of *Rhabdomys pumilio* SCN neurons.**

The day-night electrical activity and membrane excitability states of SCN neurons at the single-cell level are well characterized in nocturnal animals (Colwell, 2011; Belle & Diekman, 2018; Harvey *et al.*, 2020), but thus far there are no such measurements performed in the SCN of diurnal mammals. We therefore set out to describe the intrinsic electrical states of *R. pumilio* SCN neurons with respect to the cell’s passive membrane properties (resting membrane potential (RMP), spontaneous firing rate (SFR), and input or membrane resistance ( $R_{input}$ )), and how these change across the day and at night, using *in vitro* whole-cell patch clamp electrophysiology.

Recording (Fig.2A) from a total of 111 SCN neurons (from 8 animals) over the day-night cycle revealed four spontaneous excitability states in *R. pumilio* (Fig.2B), similar to previous descriptions in mice (Belle *et al.*, 2009; Diekman *et al.*, 2013; Paul *et al.*, 2016; Collins *et al.*, 2020). Thus, some SCN neurons were resting at moderate RMPs ( $-43.9 \pm 0.41$  mV,  $n=94/111$ ) and firing action potentials (APs). Other neurons were severely depolarized or “hyperexcited” ( $-32.7 \pm 2.36$ ,  $n=6/111$ ), to the extent that rather than generating APs, they became depolarized-silent or exhibited depolarized low-amplitude membrane oscillations (DLAMOs). The final category of neurons were hyperpolarized-silent, having RMPs too negative to sustain firing ( $-50.5 \pm 2.29$  mV,  $n=11/111$ ).

SCN neurons were overall more excited during the day than at night (Fig.2C-E), with hyperpolarized-silent neurons only appearing at night, and the daytime state being characterized by firing and depolarized cells, indicating a time-of-day control on these cellular electrical states ( $\chi^2=21.498$ ,  $p<0.001$ : Fig.2C). Accordingly, RMP and SFR showed a robust circadian variation (Fig.2D-E). During the day, SCN neurons were overall resting at more depolarized RMP, generating APs at a higher rate. This indicates that, as in nocturnal species (Belle *et al.*, 2009; Belle & Piggins, 2017), cellular RMP in the diurnal *R. pumilio* SCN is a strong determinant of electrical states and SFR. To directly test this, we subjected depolarized-silent SCN neurons to progressive steps of steady-state suppressive (negative) currents (from 0 to  $\sim -16$  pA; driving RMP from -32mV to -60mV), to see if we could elicit the range of spontaneous electrical behaviours seen in SCN neurons. Indeed, *R. pumilio* SCN neurons could be easily driven to transit from the depolarized- through to hyperpolarized-silent states, switching to DLAMOs and firing activity at appropriate RMPs in the process (Fig. 2G).

Measurement of  $R_{input}$  values showed a range from 0.84 to 4.23 G $\Omega$ , skewed towards high values, as reported in other species (Pennartz *et al.*, 1998; Jackson *et al.*, 2004; Kuhlman & McMahon, 2004; Belle *et al.*, 2009). However, we found neither a significant day-night variation in this measure (Mann-Whitney  $U=1966$ ,  $p>0.05$ , Fig.2F) nor a correlation with RMP ( $R^2 = 0.0305$ ,  $p>0.05$ ), which stands in contrast to measurements in the SCN of nocturnal animals (de Jeu *et al.*, 1998; Kuhlman & McMahon, 2004; Belle *et al.*, 2009). This represents the first substantial difference between *R. pumilio* and mouse or rat SCN.

### **Diversity in the evoked electrical responses of *Rhabdomys pumilio* SCN neurons.**

In addition to the daily variation in intrinsic electrical activity, SCN clock function also critically relies on the integrated activity of excitatory and inhibitory synaptic signals (Albers *et al.*, 2017). These inputs originate both from within the SCN (e.g. excitation or inhibition via GABA-GABA<sub>A</sub> receptor signalling) and from other brain circuits (e.g. excitation or inhibition via glutamate, or GABA signalling). Mimicking these fast signals by depolarizing and hyperpolarizing current pulses elicits diverse electrical responses in the SCN of nocturnal animals and is useful for characterizing SCN neurons (Pennartz *et al.*, 1998; Belle *et al.*, 2009; Harvey *et al.*, 2020). Therefore, we next investigated the spiking responses of *R. pumilio* SCN neurons to inputs by challenging the cells with brief current pulses (see Methods).

When subjected to depolarizing pulses, *R. pumilio* SCN neurons exhibited electrical responses similar to those of nocturnal species: a small proportion of cells (21/102) responded with a sustained and regular train of action potentials, with no, or marginal, spike-frequency adaptation (non-adapting cells, Fig. 3A). The remaining neurons (81/102) showed some degree of frequency adaptation (Fig. 3B&C). These cells either progressively slowed firing rate and exhibited increased spike shape broadening and amplitude reduction during the pulse (adapting-firing, Fig. 3B), or fired only a few APs during the initial phase of the depolarization before entering a silent state (adapting-to-silent, Fig. 3C). We found non-adapting and adapting cells resting at similar RMPs, indicating that cellular RMP was not the determinant of response type (e.g. Fig. 3A vs C). The proportion of cells displaying each of these responses did not vary across the day-night cycle ( $\chi^2=0.324$ ,  $p>0.05$ , Fig. 3D). This suggests that, as in the mouse SCN (Belle *et al.*, 2009; Belle & Piggins, 2017), these different types of spiking behaviour likely reflect “hardwire” differences between SCN neurons, rather than time-of-day dependent variations in physiological state.

We next mimicked the effect of inhibitory signals by injecting hyperpolarizing current pulses (Fig. 3E&F). In all cases, spike firing ceased during these hyperpolarizing currents. Upon pulse termination, 67% (69/103) of *R. pumilio* SCN neurons immediately resumed normal firing or showed rebound depolarization spiking before resuming normal pre-pulse level of firing (Fig. 3E), as previously reported for mouse and rat SCN (Thomson & West, 1990; Pennartz *et al.*, 1998; Kuhlman & McMahon, 2004; Belle *et al.*, 2009). The remaining 33% (34/103) of units displayed a low-threshold spike (LTS) followed by a rebound hyperpolarization which produced a prominent delay, ranging from 160 to 1430 msec, before firing resumed (Fig. 3F-i, 6H). A high proportion of cells in this second group (73.5%; 25/34) also showed an inward rectification or depolarization “sag” (Fig. 3F) during the pulse, an electrical response that is associated with H-current activation ( $I_H$ , (Pennartz *et al.*, 1998; Atkinson *et al.*, 2011)). The hyperpolarization-evoked delay to fire and LTS response (Fig. 3F-i) have not previously been reported for SCN neurons, and thus represents another significant point of divergence in SCN neurophysiology between *R. pumilio* and, previously studied, nocturnal species.

We termed *R. pumilio* neurons with rebound firing Type-A cells (Fig. 3E), and those with delays Type-B neurons (Fig. 3F-i), to be consistent with nomenclatures previously used to identify neurons with those distinct electrical characteristics elsewhere in the brain (Burdakov & Ashcroft, 2002; Burdakov *et al.*, 2004). The relative abundance of Type-A and -B cells did not change across the day-night cycle ( $\chi^2=$ ,  $p>0.05$ , Fig. 3G), indicating that these response properties are determined by cell-type rather than time-of-day.

### **Ionic mechanisms underlying evoked electrical responses.**

A comprehensive understanding of SCN neurophysiology would encompass an appreciation of the ionic mechanisms and channel parameters responsible for the electrophysiological properties revealed in our whole-cell recordings (Belle & Diekman, 2018; Harvey *et al.*, 2020). Capturing this ionic information from current-clamp data has only recently become feasible due to advances in data assimilation (DA) techniques (Abarbanel, 2013). Here, we

developed a state-of-the-art DA algorithm (see Methods section for a detailed description) and applied it to build detailed computational models of *R. pumilio* SCN neurons (Fig.S1 & S2). This modelling approach reproduced the voltage trajectory and nuances of action potentials and subthreshold electrical activity generated during spontaneous and evoked firing of SCN neurons in remarkable detail (Fig. 4 and S2), providing confidence that the ionic currents and parameters estimated by our DA algorithm, and their dynamical relationship in the models, are indeed a close match to their biological values and activity.

Through simulations of the model, we first assessed how ionic conductances interact with each other to produce AP firing and other electrical behaviours (information that could never be obtained experimentally since current-clamp and voltage-clamp cannot be simultaneously performed). We applied this approach to compare the conductances underlying spontaneous AP generation in the *R. pumilio* SCN model (Fig.4A) to our previously published model of mouse SCN neurons (Belle *et al.*, 2009) containing the same sets of ionic currents (voltage-dependent transient sodium  $I_{Na}$ , voltage-dependent transient calcium  $I_{Ca}$ , voltage-dependent potassium  $I_K$ , and voltage-independent leak,  $I_L$ ). We found that the overall profile of how these currents contribute to AP generation is similar across the two species (Fig.S3). In addition, the types of bifurcations at the transitions between rest states and spiking are the same in both models (subcritical Hopf from hyperpolarized silent to spiking, and supercritical Hopf from depolarized-silent to spiking), suggesting the qualitative dynamics that lead to repetitive AP firing are similar across the two species (Fig. S4A). Furthermore, the *R. pumilio* model can produce all the electrical behaviours observed across the day-night cycle (depolarized-silent, DLAMOs, fast-firing, slow-firing, and hyperpolarized-silent, Fig. S4B-F) through an antiphase circadian rhythm in sodium and potassium leak currents, consistent with the “bicycle model” proposed for the circadian regulation of electrical activity in mice and flies (Flourakis *et al.*, 2015).

We next used the model to gain insight into the mechanisms responsible for the adapting versus non-adapting firing behaviours observed in response to depolarizing pulses. Our DA algorithm yielded models that faithfully reproduced the voltage traces and spike shapes from non-adapting, adapting-firing, and adapting-to-silent cells (Fig. 5A-B). By inspecting the ionic currents flowing during the simulated voltage traces, we assessed the role of voltage-gated sodium  $I_{Na}$ , calcium  $I_{Ca}$ , and potassium  $I_K$  currents in producing these responses (Fig. 5C).

Our models revealed that frequency adaptation in SCN neurons in response to excitation resulted from the progressive inactivation of sodium channels. Indeed, the adapting-firing model indicated a much smaller amount of  $I_{Na}$  available for the APs during the depolarizing pulse (peak  $I_{Na} = -80$  pA, Fig. 5Cii), and a greater reduction in sodium conductance  $G_{Na}$  (26 nS before vs 1.5 nS during the pulse, Fig. 5Dii) compared with the non-adapting model (peak  $I_{Na} = -580$  pA;  $G_{Na} = 27$  nS before vs 13 nS during the pulse, Fig. 5Ci & Di). Remarkably however, increased sodium channel inactivation ( $h_{Na}$  close to 0) could not be ascribed to intrinsic differences in the sodium channel properties themselves between the non-adapting and adapting-firing models as the kinetic parameters of the sodium activation and inactivation gating variables were similar (Fig.5F-G). Rather, the difference was due to differing properties of the potassium channels. A combination of a flattened steady-state potassium activation ( $n_\infty$ ) curve (Fig. 5H) and the lower  $g_K$  value (Fig. 5I), led to a smaller  $I_K$  and reduced  $G_K$  during AP firing in the adapting-firing compared to the non-adapting model (250 pA, 3 nS vs 900 pA, 11 ns, respectively) (Fig.5C-D i-ii). Since  $I_K$  is an outward current, this means that the adapting-firing model does not repolarize as strongly after the peak of an AP, and therefore, the membrane does not hyperpolarize enough to de-inactivate the sodium channels. Thus, in the adapting-firing model, the inability of a weak  $I_K$  to sufficiently repolarize the membrane is what ultimately leads to the reduced  $I_{Na}$  and low-amplitude APs. The  $I_K$  is even smaller in the adapting-to-silent model (Fig. 5Ciii), failing to repolarize the membrane, and leads to sustained inactivation of the sodium channel (Fig. 5Eiii), negligible sodium conductance (Fig. 5Diii) and ultimately the inability to repeatedly fire APs during the

pulse (Fig. 5Biii). In summary, our models support progressive sodium channel inactivation as the mechanism of frequency adaptation (consistent with experimental observation in neurons elsewhere in the brain (Fleidervish *et al.*, 1996; Jung *et al.*, 1997; Kimm *et al.*, 2015) and our previously published model of mouse SCN neurons (Belle *et al.*, 2009)), while indicating that this is primarily a consequence of a weak  $I_K$ .

We next interrogated our models for the key ionic origins of Type-A vs Type-B responses to inhibition (Fig. 3E&F). In both cell types, hyperpolarizing pulses drove the membrane potential in the real and model cells below the firing threshold, which suppressed firing activity during the pulse (Fig. 6A-B, i-ii). Model analysis showed that in the Type-A cell, the  $I_{Na}$  and  $I_{Ca}$  currents were larger during the first AP immediately following the pulse than during the APs before the pulse (Fig. 6D), leading to a high-amplitude rebound spike. The rebound spiking was due to sodium and calcium ion channels becoming completely de-inactivated ( $h_{Na}$  and  $h_{Ca}$  both approach 1) at the hyperpolarized membrane potential reached during the pulse (Fig. 6F). The time scale of calcium ion channel inactivation causes  $I_{Ca}$  to remain elevated for a few hundred milliseconds after the pulse, resulting in a transient after-depolarization and a short burst of firing before returning to the baseline pre-pulsed spike rate (Fig. 6A).

Similar  $I_{Na}$  and  $I_{Ca}$  dynamics were present in the Type-B neuron model. However, the rebound hyperpolarization and prominent delay-to-fire after the pulse observed in Type-B neurons (Fig. 3F and 6Bi-ii), was not possible to reproduce using our existing basic model (Fig. 4A), consistent with the failure to observe such behaviour in the mouse SCN. It is well established in neurons elsewhere in the brain that the inhibitory actions of the transient subthreshold activating A-type ( $I_A$ ) voltage-gated potassium channels ( $K_v$ ) underpin such delay-to-fire activity (Schoppa & Westbrook, 1999; Saito & Isa, 2000; Burdakov & Ashcroft, 2002; Burdakov *et al.*, 2004; Nadin & Pfaffinger, 2010). Another feature of Type-B activity that could not be recreated with our basic model was the prominent depolarization “sag” seen in the voltage trace during the pulse (Fig. 3F and 6Bi). Such behaviour could be produced by activation of an  $I_H$  current by the hyperpolarizing pulse. We therefore added  $I_A$ , as well as a hyperpolarization-activated ( $I_H$ ) current, to our mouse SCN model in an attempt to recreate the voltage trace and biophysical condition of the Type-B neuron (Fig. 6C).

The expanded model revealed a larger  $I_A$  current during the first APs after the delay (480 pA) than during a typical spike (220 pA, Fig. 6E). Importantly, there was also 15 pA of  $I_A$  current flowing during the delay itself (Fig. 6E inset). It is noteworthy that this was greater than the 5 pA of  $I_A$  current that flows during the inter-spike interval. This enhanced  $I_A$  current following the pulse was due to de-inactivation of the A-type channel ( $h_A$  approaches 1) during the hyperpolarizing pulse (Fig. 6G), rendering the  $I_A$  channel fully available upon release of the pulse, an observation that is consistent with experimental findings (Burdakov *et al.*, 2004). The  $I_A$  current then inactivates slowly and, until this outward current decays sufficiently, the cell cannot reach threshold to fire, thereby prolonging inhibition. This inhibition-supportive action of  $I_A$  is consistent with observations made elsewhere in the brain (Burdakov & Ashcroft, 2002; Burdakov *et al.*, 2004), and previous simulations (Rush & Rinzel, 1995; Patel *et al.*, 2012).

It has previously been shown that variation in cellular  $I_A$  conductances and inactivation time constant can impact time to fire (e.g. (Saito & Isa, 2000)), and this may explain the broad range in the delay-to-fire, from 160 to 1430 msec, seen in our Type-B neurons (Fig. 6H). Indeed, this was the case in our model. By varying the maximal  $I_A$  conductance (Fig. 6I&J) and inactivation time constant (Fig. 6M &N) parameters, we were able to capture the full range of latency to fire seen in Type-B cells, with higher conductances and longer inactivation time constants producing longer delays. Complete removal of the  $I_A$  conductance eliminated the delay and produced a Type-A response (Fig. 6Ji-iii), reinforcing the different ionic composition of these two cell types.

In summary, our revised model was able to mirror all the electrical features observed in *R. pumilio* SCN neurons in response to extrinsic inputs, and identified transient subthreshold A-type potassium channels as playing a key role in evoked-suppression firing in simulated SCN neurons.

### **$I_A$ currents suppress firing under physiological simulation.**

We finally interrogated our model to understand how the  $I_A$  conductances required to explain SCN responses to hyperpolarizing pulses may impact firing activity in a more realistic neurophysiological setting. To this end, we first subjected the model to simulated synaptic conductances recorded from *R. pumilio* SCN neurons (Fig. S5). To account for the ability of the SCN's major neurotransmitter (GABA) to be either inhibitory or excitatory (Albers *et al.*, 2017), we applied GABAergic synaptic conductances of either polarity ( $g_{syn-I}$  and  $g_{syn-E}$ ). Our simulations showed that overall, in the absence of GABAergic synaptic conductance ( $g_{syn-I} = 0$  nS),  $I_A$  led to a suppression of spontaneous firing rate in model SCN neurons (Fig. 7 A&B, a1 vs a4). This observation is consistent with previous experimental work (Granados-Fuentes *et al.*, 2012; Hermanstyne *et al.*, 2017). This effect was retained following inclusion of synaptic input of either polarity (Fig. 7A-B, compare a2 vs a5, and a3 vs a6), with the suppressive effect of  $g_{syn-I}$  especially augmented by high  $I_A$  (Fig. 7B).

Having observed such effects of  $I_A$  on intrinsic activity and cellular response to inputs, we next investigated its effects on the spontaneous activity exhibited by SCN neurons across the circadian day. Here, we simulated the different resting states of *R. pumilio* SCN neurons and day-night changes in spontaneous firing rate (as in the neurons, Fig. 2B&E, respectively) by subjecting the model to a range of leak currents. Specifically, we varied the scaling factor for the ratio of potassium leak ( $g_{LK}$ ) to sodium leak ( $g_{LNa}$ ) from 0.85 to 1.15 (Fig. 7C). This was motivated by previous work showing that sodium leak current is higher during the day than at night in mouse SCN neurons (Flourakis *et al.*, 2015). Furthermore, it has been suggested that potassium leak currents are lower during the day and higher at night. According to this “bicycle” model, a  $g_{LK}/g_{LNa}$  scaling factor less than 1 corresponds to a daytime “up-state”, and a scaling factor greater than 1 to a night-time “down-state”. Simulating this variation in leak currents indeed transited the spontaneous RMP and firing rate of the model cells from the daytime depolarized state to night-time suppressed state (as in the neurons, Fig. 2B&G; Fig. S4B-F). We then tested the influence of  $I_A$  on firing rate at each of these electrical states. As reported above, our results revealed that, overall,  $I_A$  conductances suppressed spontaneous firing activity (Fig. 7C, c1-c3), but the extent of this suppression was magnified in slow firing and more hyperpolarized cells (Fig. 7C, c3), such as those frequently recorded at night.

Altogether, these observations are consistent with experimental findings in the SCN, and elsewhere in the brain, that  $I_A$  conductances assist suppressive signals. We therefore conclude that in the *R. pumilio* SCN,  $I_A$  conductances may act as a “break” to modulate (tone down) excitation during the day in depolarized excited cells, and promote inhibition at night in more hyperpolarized slow-firing neurons.

## **DISCUSSION**

We have applied whole-cell recordings, advanced data assimilation and modelling approaches to provide the first comprehensive description of spontaneous, and evoked, electrical activity of individual SCN neurons in a diurnal species. Our approach reveals strong similarities with the SCN of closely related nocturnal species, but also notable differences.

### Similarities with the nocturnal SCN

Most importantly, the fundamental daily rhythm in electrical excitability ('upstate' during the day and a 'downstate' at night (Allen *et al.*, 2017; Belle & Diekman, 2018; Harvey *et al.*, 2020)) reported for nocturnal species is retained in *R. pumilio*. This reinforces the current view that mechanisms of rhythm generation and regulation are broadly retained across mammalian species with different circadian niches. Moreover, the response of *R. pumilio* SCN neurons to depolarizing inputs and the underlying ionic mechanisms were similar to that of nocturnal rodents (Belle *et al.*, 2009). In further support of this view, our modelling revealed similar action potential generation mechanisms in the *R. pumilio* SCN to those in the mouse and rat SCN (Jackson *et al.*, 2004; Belle *et al.*, 2009).

### Novel properties of the *Rhabdomys pumilio* SCN

The most obvious point of divergence between the *R. pumilio* SCN and that of closely related nocturnal species was its response to hyperpolarizing pulses. Thus, we found that a substantial fraction of *R. pumilio* neurons showed a prominent delay-to-fire (for several hundreds of milliseconds in some cells) following inhibitory pulses. This sort of electrical reaction to inhibition has been observed in neurons elsewhere in the brain (Schoppa & Westbrook, 1999; Saito & Isa, 2000; Burdakov & Ashcroft, 2002; Burdakov *et al.*, 2004; Nadin & Pfaffinger, 2010), but to the best of our knowledge has never before been reported in SCN neurons (Thomson & West, 1990; Pennartz *et al.*, 1998; Kuhlman & McMahon, 2004; Belle *et al.*, 2009; Gamble *et al.*, 2011; Belle & Piggins, 2017). The appearance of such 'Type-B' neurons in the SCN is thus a novel property of *R. pumilio*.

What causes delay-to-fire activity in *R. pumilio* neurons (and why are they absent from the nocturnal SCN)? Our computational models identified the activity of the transient subthreshold A-type potassium channels ( $I_A$ ) as the likely determinant of this suppressive bioelectrical effect, with the  $I_A$  conductance density (which presumably represents the number of functional  $I_A$  channels), defining the delay-to-fire latency. The implication, that cells with higher  $I_A$  conductances show longer delay-to-fire latencies, finds support from experimental findings elsewhere in the brain (Schoppa & Westbrook, 1999; Saito & Isa, 2000; Burdakov & Ashcroft, 2002; Burdakov *et al.*, 2004; Nadin & Pfaffinger, 2010).

The pore-forming ( $\alpha$ ) subunits of  $I_A$  channels (Kv1.4, 4.1, 4.2 and 4.3) are present in nocturnal rodent (rat, mouse and hamster) SCN neurons, and have been implicated in regulating electrical activity and supporting core clock function (Huang *et al.*, 1993; Bouskila & Dudek, 1995; Alvado & Allen, 2008; Itri *et al.*, 2010; Granados-Fuentes *et al.*, 2012; Granados-Fuentes *et al.*, 2015; Hermanstyne *et al.*, 2017). Their failure to produce the delay-to-fire phenotype in those nocturnal species therefore likely reflects some quantitative variation in their function. A likely possibility, consistent both with known features of  $I_A$  physiology and our modelling of the *R. pumilio* SCN, is variation in inactivation time constant (timescale over which a channel becomes inactivated following de-inactivation). Elsewhere in the brain it has been shown experimentally that cells expressing  $I_A$  channels with faster inactivation time constants (close to 12 ms) show rebound firing, while slower inactivation time constants (~140 ms) produce delay-to-fire activity (Saito & Isa, 2000; Burdakov *et al.*, 2004). Interestingly, the  $I_A$  inactivation time constant measured in mouse and hamster SCN neurons showed relatively fast gating variables (below 22 ms: (Alvado & Allen, 2008; Itri *et al.*, 2010)), consistent, therefore, with the presence of rebound but not delay-to-fire characteristics in SCN neurons of these species. In agreement, to fully model the range of delay-to-fire behaviours observed in *R. pumilio* SCN neurons, our original mouse model had to be supplemented with  $I_A$  channels with a slow inactivation time constant (near 140 ms) (Fig. 6C,J&N). Variation in delay-to-fire appeared due to alteration in  $I_A$  conductances (Fig. 6I&J), however, the range of delay latencies observed in our recordings could also be produced by varying the inactivation time constant while holding the  $I_A$  conductance constant (Fig. 6M&N). The inactivation time constants returned by this modelling fall within physiological ranges, and values required to produce delay-to-fire responses are similar to

experimentally determined values in other parts of the brain (Saito & Isa, 2000; Burdakov *et al.*, 2004).

The functional properties of the  $I_A$  channel family (Kv4), specifically inactivation time constant and current density, can be influenced by two classes of auxiliary proteins known as Kv channel-interacting proteins (KChIP1–4) and dipeptidyl peptidase-like proteins (DPLPs; DPP6 and DPP10) (Jerng & Pfaffinger, 2014). When associated with the various complements of these proteins, the  $I_A$  channel inactivation time constant can vary from a few ms to several hundred ms (depending on their expression pattern and the nature of interaction with the channels), reversibly transforming rebound firing to delay firing cells (Shibata *et al.*, 2000; Holmqvist *et al.*, 2002; Jerng *et al.*, 2004; Jerng *et al.*, 2005; Jerng *et al.*, 2007; Amarillo *et al.*, 2008; Maffie *et al.*, 2009; Nadin & Pfaffinger, 2010). The transcripts for these auxiliary proteins are expressed brain-wide across different mammals, including in the SCN of nocturnal rodents (Wen *et al.*, 2020) and the diurnal baboon (Mure *et al.*, 2018), and have been implicated in circadian control mechanisms in other excitable cell types (Jeyaraj *et al.*, 2012).

A plausible explanation for the range of delay-to-fire activity in the *R. pumilio* SCN, therefore, is variation in activity of KChIP and DPLP proteins producing diversity in inactivation time constants. Interestingly, such a mechanism could also account for the other notably unusual feature of the *R. pumilio* SCN - the absence of a clear relationship between RMP and  $R_{input}$  (Figure 2F). These  $I_A$  auxiliary proteins are known to regulate the input resistance ( $R_{input}$ ) of neurons without changing resting membrane potential (RMP) and capacitance (Nadin & Pfaffinger, 2010). Thus, variation in KChIP and DPLP activity across the population of *R. pumilio* SCN neurons could both produce diversity in delay-to-fire activity and disrupt the link between RMP and  $R_{input}$  across neurons observed in nocturnal species (Kuhlman & McMahon, 2004; Belle *et al.*, 2009).

### Putative functional significance

We applied modelling to determine how  $I_A$  channels may regulate excitability in *R. pumilio* SCN neurons in the face of spontaneous (circadian) variations in intrinsic neuronal properties and synaptic input. Experimental results in nocturnal SCN (Granados-Fuentes *et al.*, 2012; Hermanstyne *et al.*, 2017) and elsewhere in the brain (Connor & Stevens, 1971; Rudy, 1988; Liss *et al.*, 2001; Baranauskas, 2007; Khaliq & Bean, 2008) reveal that  $I_A$  channels can suppress spontaneous firing rate. Our modelling returned a similar impact of  $I_A$  in *R. pumilio*, while revealing aspects of this effect that could be especially relevant for a diurnal species. Thus, in general,  $I_A$  reduced the effect of intrinsic or synaptically-driven increases in excitability on firing, while enhancing the impact of inhibitory currents (Fig. 7). The weight of this effect though fell differently across the circadian cycle.

In our model, the weight of the imposed suppression of firing by  $I_A$  conductances was stronger at night (in hyperpolarized low-firing neurons) than in the day (in more depolarized fast-firing neurons) (Fig. 7). In this way,  $I_A$  would reinforce the SCN's 'down-state' at night. In nocturnal species, the intrinsic reduction in SCN activity at night is augmented by the appearance of inhibitory inputs associated with activity and arousal at this circadian phase (van Oosterhout *et al.*, 2012). Such inhibitory inputs are presumably reduced in diurnal species such as *R. pumilio*, in which activity occurs predominantly during the day. The biophysical properties of  $I_A$  channels (conductance active at the subthreshold range of the RMP and progressively becoming available with hyperpolarization), together with its sensitivity to neurotransmitters (Aghajanian, 1985; Yang *et al.*, 2001; Burdakov & Ashcroft, 2002), could provide an opportunity for the *R. pumilio* SCN to compensate for the reduction in inhibitory inputs at night. Accordingly, our modelling evidence favours the interpretation that  $I_A$  acts to amplify suppressive signals at night to maintain the low electrical activity in the SCN at this time of day.

The  $I_A$  conductance may also be an important response to enhanced excitatory inputs during the day in diurnal species. Day-active animals are exposed to daytime light (the most important excitatory input to the SCN) to an extent that nocturnal species are not. The ability of  $I_A$  to reduce the impact of such excitatory inputs, and perhaps augment the effect of inhibitory inputs from the thalamus, lateral hypothalamus or retina (Belle *et al.*, 2014; Sonoda *et al.*, 2020) or intrinsic to the SCN (Hannibal *et al.*, 2010), would apply an appropriate 'brake' on daytime activity of the SCN.

In summary, our whole-cell recordings and computational modelling highlight the potential importance of  $I_A$  in tuning excitability in the *R. pumilio* SCN. This may be an important step in accommodating SCN activity to diurnal living while maintaining the day/night contrast in electrical activity necessary for health and wellbeing.

### Applying the data assimilation method to physiology

Our results demonstrate that data assimilation (DA) is a powerful tool for developing conductance-based models. Our state-of-the-art DA algorithm was able to reliably perform state and parameter estimation for *R. pumilio* SCN neuron models from current-clamp recordings without the use of voltage-clamp and pharmacological agents to isolate specific currents, and without the injection of custom-designed stimulus waveforms as used in other DA approaches (Meliza *et al.*, 2014). Rather, we made judicious use of the voltage traces resulting from standard depolarizing and hyperpolarizing current steps. This is an important step forward for the practicality of applying DA methodology in the neuroscience context, as it enables model-building from the plethora of past, present, and future current-clamp recordings obtained by electrophysiology labs using classical current-step protocols.

## METHODS

### Animals

All animal use was in accordance with the UK Animals, Scientific Procedures Act of 1986, and was approved by the University of Manchester Ethics committee. Adult *R. pumilio* (male and female, age 3-9 months) were housed under a 12:12h light dark cycle (14.80 Log Effective photon flux/cm<sup>2</sup>/s for melanopsin or Melanopic EDI (equivalent daylight illuminance) of 1941.7 lx) and 22°C ambient temperature in light tight cabinets. Food and water were available *ad libitum*. Cages were equipped with running wheels for environmental enrichment. Zeitgeber Time (ZT) 0 corresponds to the time of lights on, and ZT12 to lights off.

### Brain slice preparation for electrophysiological recordings

Following sedation with isoflurane (Abbott Laboratories), animals were culled by cervical dislocation during the light phase (beginning of the day or late day). Brains were immediately removed and mounted onto a metal stage. Brain slices were prepared as described previously (Hanna *et al.*, 2017). 250 $\mu$ m coronal slices containing mid-SCN levels across the rostro-caudal axis were cut using a Campden 7000smz-2 vibrating microtome (Campden Instruments, Loughborough, UK). Slices were cut in an ice-cold (4°C) sucrose-based incubation solution containing the following (in mM): 3 KCl, 1.25 NaH<sub>2</sub>PO<sub>4</sub>, 0.1 CaCl<sub>2</sub>, 5 MgSO<sub>4</sub>, 26 NaHCO<sub>3</sub>, 10 D-glucose, 189 sucrose, oxygenated with 95% O<sub>2</sub>, 5%CO<sub>2</sub>. After slicing, tissue was left to recover at room temperature in a holding chamber with continuously gassed incubation solution for at least 20 min before transferring into recording aCSF. Recording aCSF has the following composition (mM): 124 NaCl, 3 KCl, 24 NaHCO<sub>3</sub>, 1.25 NaH<sub>2</sub>PO<sub>4</sub>, 1 MgSO<sub>4</sub>, 10 D-Glucose and 2 CaCl<sub>2</sub>, and 0 sucrose; measured osmolarity of 300-310 mOsmol/kg. Slices were allowed to rest for at least 90 min before starting electrophysiological recordings.

### Whole-cell patch clamp recordings

SCN brain slice electrophysiology was performed as previously described (Belle *et al.*, 2014). SCN coronal brain slices were placed in the bath chamber of an upright Leica epifluorescence microscope (DMLFS; Leica Microsystems Ltd) equipped with infra-red video-enhanced differential interference contrast (IR/DIC) optics. Brain slices were kept in place with an anchor grid, and continuously perfused with aCSF by gravity (~2.5ml/min). Recordings were performed from neurons located across the whole SCN during the day and at night (Fig. 2A). SCN neurons were identified and targeted using a 40x water immersion UV objective (HCX APO; Leica) and a cooled Teledyne Photometrics camera (Retiga Electro), specifically designed for whole-cell electrophysiology. Photographs of the patch pipette sealed to SCN neurons were taken at the end of each recording for accurate confirmation of anatomical location of the recorded cell within the SCN.

Patch pipettes (resistance 7–10MΩ) were fashioned from thick-walled borosilicate glass capillaries (Harvard Apparatus) pulled using a two-stage micropipette puller (PB-10; Narishige). Recording pipettes were filled with an intracellular solution containing the following (in mM): 120 K-gluconate, 20 KCl, 2 MgCl<sub>2</sub>, 2 K<sub>2</sub>-ATP, 0.5 Na-GTP, 10 HEPES, and 0.5 EGTA, pH adjusted to 7.3 with KOH, measured osmolarity 295–300 mOsmol/kg.

An Axopatch Multiclamp 700A amplifier (Molecular Devices) was used for voltage-clamp and current-clamp recordings. Pipette tip potential was zeroed before establishing membrane-pipette giga-ohm seal, and cell membrane was ruptured under voltage-clamp mode at -70 mV using minimal negative pressure. Signals were sampled at 25 kHz and appropriately acquired in gap-free or episodic stimulation mode using pClamp 10.7 (Molecular Devices). Series resistance (typically 10–30 MΩ) was corrected using bridge-balance in current-clamp experiments and was not compensated during voltage-clamp recordings. Access resistance for the cells used for analysis was <30 MΩ. Post-synaptic currents (PSCs) were measured under voltage-clamp mode while holding the cells at -70mV. Measurement of spontaneous activity in current-clamp mode was performed with no holding current (I=0). All data acquisition and protocols were generated through a Digidata 1322A interface (Molecular Devices). Recordings were performed at room temperature (~ 23°C). A portion of the data appearing in this study also contributed to the investigation of the impact of daytime light intensity on the neurophysiological activity and circadian amplitude in the *R. pumilio* SCN (Bano-Otalora *et al.*, 2020)

### Membrane properties of SCN neurons

Resting membrane potential (RMP), spontaneous firing rate (SFR) and input resistance ( $R_{\text{input}}$ ) were determined within 5 min of membrane rupture. Average SFR in firing cells was calculated as the number of action potentials per second within a 30s window of stable firing using a custom-written Spike2 script, and average RMP was measured as the mean voltage over a 30s window.  $R_{\text{input}}$  was estimated using Ohm's law ( $R=V/I$ ) where V represents the change in voltage induced by a hyperpolarizing current pulse (-30pA for 500 ms) as previously described (Belle *et al.*, 2009). The neurone's response to excitatory and inhibitory stimuli was identified by a series of depolarizing and hyperpolarizing current pulses (from -30 to +30pA in 5pA steps, duration 1s).

### Immunohistochemistry

*R. pumilio* were culled during the light phase and brains were fixed in 4% PFA, followed by 5 days in 30% sucrose. 35μm brain sections were cut using a freezing sledge microtome (Bright Instruments, Huntingdon, UK). Immunofluorescence staining was performed as previously described (Timothy *et al.*, 2018). Briefly, slices were washed in 0.1M PBS and 0.1% TritonX-100 in PBS before incubation with blocking solution (5% donkey serum (Jackson ImmunoResearch, Pennsylvania, US) in 0.05% Triton-X100 in 0.1M PBS). After 60 min, sections were incubated for 48h at 4°C with primary antibodies (AVP Rabbit, Millipore AB1565, 1:5000; VIP Rabbit, Enzo, VA1280-0100, 1:1000; GRP Rabbit, Enzo GA1166-0100, 1:5000). Following washes, slices were incubated overnight with secondary antibodies

(1:800; Donkey anti-rabbit Cy3, Jackson ImmunoResearch). Slices were finally mounted onto gelatine coated slides and cover-slipped using DAPI-containing Vectashield anti-fade media (Vector Laboratories, Peterborough, UK). Digital photos were taking using a Leica DFC365 FX camera connected to a Leica DM2500 microscope using Leica Microsystems LAS AF6000 software.

### Data analysis

Current-clamp data were analysed using Spike2 software (Cambridge Electronic Design, CED). Non-normal distributed electrophysiological data from different time-of-day were compared using Mann-Whitney U Test. All statistical analyses were performed using SPSS version 23 (SPSS Inc., Chicago, IL, USA) and GraphPad Prism 7.04 (GraphPad Software Inc., CA, USA). For all tests, statistical significance was set at  $p < 0.05$ . Data are expressed as mean  $\pm$  SEM. Sample sizes are indicated throughout the text and figure legends. Percentages of cells in the different electrophysiological states and responses to depolarizing and hyperpolarizing pulses during the day and at night were analysed using Chi-Squared test.

### Model estimation strategy

Traditionally, conductance-based (or Hodgkin-Huxley-type) models of neurons are constructed using voltage-clamp (VC) measurements of individual ionic currents. While VC can provide accurate descriptions of certain channel properties, its execution is experimentally labour intensive, and by measuring each current in isolation VC protocols do not capture the dynamical interplay between the many active channels that drive complex and integrated electrical behaviours in mammalian neurons. Furthermore, it is not feasible to use VC to measure all the ionic currents of interest from the same cell, due to the limited amount of time available to perform patch-clamp recordings before the cell dialyzes (approximately 5 to 10 minutes) and the need to wash out the pharmacological agents used to isolate and measure one current before isolating and measuring the next. Thus, a model constructed using VC data is not a representation of the currents active in a single cell, but rather is a combination of currents measured across several different cells (Golowasch *et al.*, 2002).

The advantage of current-clamp (CC) protocols is that the recorded voltage trace reflects the natural interaction of all the ionic conductances within that cell. The challenge for constructing a model based on CC data is that only one of the state variables of the model, the membrane voltage, has been measured directly; the gating variables that represent the opening and closing of ion channels are unobserved. Each ionic current has several parameters associated with it that are typically not known *a priori* and must also be estimated from the data.

Data assimilation is widely used in fields such as geoscience and numerical weather prediction but has only recently begun to be applied in neuroscience. One of the main classes of DA algorithms are variational methods such as 4D-Var that seek solutions through optimization over a time window and are able to deal more effectively with a large number of unobserved state variables and unknown parameters. Since our *R. pumilio* SCN model has many parameters that are not known *a priori* we chose to employ the variational approach in this study.

A variational data assimilation algorithm was used to perform model fitting. We used current-clamp data from multiple protocols (Fig. S1) simultaneously to inform the estimated model of robust responses to changes in the applied current. We initially used a set of channels in our *R. pumilio* model similar to that previously used for a mouse SCN model (Belle *et al.*, 2009) (Fig. 4A), but permitted each of the parameters in the model the freedom to be distinct for each individual cell that we fit. We started the estimation algorithm for each cell using over

50 initial guesses for the parameters and state variables, and performed model selection by assessing a Pareto frontier consisting of the DA cost function evaluation and the mismatch in firing rate between the model output and the data for simulations the resulting model under various current-clamp conditions. These simulations were preformed using the `ode15s` and `ode45` solvers in MATLAB.

### Data assimilation algorithm

Here we briefly describe the variational DA algorithm employed in this paper (see (Moye, 2020) for further details). We represent the neuronal recordings using the following state-space description:

$$\begin{aligned} x_{k+1} &= f(x_k) + \omega_{k+1}, & x_k \in R^L \\ y_{k+1} &= V_{k+1} + \eta_{k+1}, & y_k \in R^1 \end{aligned}$$

where  $x_k$  is interpreted as the state of the neuron at some time  $t_k$  and  $y_k$  are our observations (i.e. the voltage measurements). The random variables  $\omega_k$  and  $\eta_k$  represent model error and measurement error, respectively. We assume that  $\omega_k \sim \mathcal{N}(0, Q)$  and  $\eta_k \sim \mathcal{N}(0, R)$ , where  $Q$  and  $R$  are the model error and measurement error covariance matrices, and that these have no cross-covariance.

*Strong 4d-var* forces our observations to be consistent with the model,  $f$ . This can be considered the result of taking  $Q \rightarrow 0$ , which yields the nonlinearly constrained problem:

$$C(x) = \frac{1}{2} \sum_{k=0}^N R^{-1}(y_k - V_k)^2$$

such that

$$x_{k+1} = f(x_k), \quad k = 0 \dots N$$

where  $R^{-1}$  can now be scaled out completely.

In the cost function, the estimated voltage is expected to be consistent with the dynamics for large model weighting  $Q^{-1}$ , but the dynamics cannot possibly reproduce the irregularity in the data.

Dynamical State and Parameter Estimation (DSPE) is a technique described by Abarbanel et al. (2009) (Abarbanel, 2009), with the premise being to stabilise the synchronization manifold of data assimilation problems by adding a control or “nudging” term  $u$ . The cost function then becomes:

$$C(x) = \frac{1}{2} \sum_{k=0}^N R^{-1}(y_k - V_k)^2 + \sum_{k=0}^N u_k^2$$

This synchronization procedure has also been considered for specific function forms of  $u$  in the neuroscience context in (Brookings et al., 2014) wherein they set up an optimal search strategy applied to real data. The nudging strategy in general has been used in geosciences primarily for state estimation (Park, 2013). As shown in Toth et al. (2011) (Toth et al., 2011) and Abarbanel et al. (2009) (Abarbanel, 2009), the control  $u$  acts to reduce conditional Lyapunov exponents.

The goal of DSPE is to define a high-dimensional cost functional which weakly constrains the estimated states to the system observations, and strongly constrains the estimates to the controlled model dynamics while penalizing the control. Without the control, the problem is explicitly formulated as a strong constraint 4D-Var. However, the basin of attraction for global minima along the optimization manifold is shallow. Also, while the minimization term itself is convex, the nonlinearities present in the model constraints generate a large degree of non-convexity in the solution manifold. The intended effect of the nudging term is to

smoothen the surface. Given that the system is so high dimensional and tightly coupled, formally visualizing this surface is not achievable for our parameter estimation problems.

In the DSPE framework, parameters and states at each point in time are taken on equal footing. Namely, the solution space of the cost function is  $(L + 1)(N + 1) + D$  where  $D$  is the number of fixed parameters to infer and  $L$  is the number of dynamical variables. Additionally, we are solving for the control  $u(t)$  at each point in time. The control is penalised quadratically in an effort to reduce the impact of it at the end of the optimization procedure. While having the control present enforces the data in the model equations, by minimizing it, one is attempting to recover back the minima subject to the uncontrolled model of the system. So, as  $u \rightarrow 0$  over the course of the optimization, the physical system strong constraint is recovered. We note that in the results presented here, the control term was not fully eliminated by the end of the assimilation window. This may be due to intrinsic voltage-gated conductances present in the cell that are not included in our model, or other factors such as synaptic input or channel noise.

We must choose a particular transcription method to prescribe our equality constraints. We define our state vector as  $x = (V, \bar{x})$  and our uncontrolled dynamics as:

$$\frac{dx}{dt} = f_x(x, \theta)$$

where we can separate out the terms with observations. We assume we only have observations of the voltage of one cell in one compartment (with natural generalizations to networks and multi-compartment descriptions):

$$\begin{aligned} \frac{dV}{dt} &= f_V(\bar{x}, V; \theta) \\ \frac{d\bar{x}}{dt} &= f_{\bar{x}}(\bar{x}, V; \theta). \end{aligned}$$

Then our controlled dynamics become

$$\begin{aligned} \frac{dV}{dt} &= f_V(\bar{x}, V; \theta) + u(V_{obs} - V) \\ \frac{d\bar{x}}{dt} &= f_{\bar{x}}(\bar{x}, V; \theta) \end{aligned}$$

where it is understood that  $u(t)$  appears only at observational times.

We can formulate the constraints using either a multiple-shooting style approach or using collocation. We will assume measurements are taken uniformly at  $t_k = t_0 + k\tau_{obs}$ . High resolution measurements are preferred so that we can have control and knowledge of the system at basically every knot point. However, there are circumstances where we may not have data with that level of precision, or we may desire to downsample our data. For that reason, we will say that we have a set of times upon which our constraint equations are satisfied, namely  $t_m = t_0 + m\tau_{col}$  where we simply require that the ratio of these time differences is a positive integer,  $\frac{\tau_{obs}}{\tau_{col}} \in \mathbb{N}$ .

To reiterate, the constraints are what connect each of our time points  $[t_m, t_{m+1}]$  to one another.

We use a direct collocation method due to the stability options afforded to us for our highly complex, nonlinear problem. With collocation, implementation of implicit methods is effectively as simple as explicit methods. We choose to use Hermite-Simpson collocation which approximates the set of discrete integrations using Simpson's rule. We introduce midpoints in this fashion  $(x_{k+\frac{1}{2}})$ , which are approximated using Hermite interpolation.

$$x_{k+1} - x_k = \frac{1}{6} h_k \left( f_k + 4f_{k+\frac{1}{2}} + f_{k+1} \right)$$

$$x_{k+\frac{1}{2}} = \frac{1}{2}(x_k + x_{k+1}) + \frac{h_k}{8}(f_k - f_{k+1})$$

where  $f_k = f_x(x_k, \hat{\theta})$  and  $\hat{\theta}$  is the present estimate of  $\theta$  constant across our time window.

Here, we take the midpoint and endpoint conditions on equivalent footing for our constraints,  $g(x) = 0$ , in what is known as its ``separated form''. Therefore, we implement these equations so that  $h_k = 2\tau_{col}$  based upon our previous notation, and we have  $LN$  equality constraints.

### State and parameter bounds

Setting lower and upper bounds for the state and parameter estimates,  $x^L \leq x \leq x^U$ , can improve the performance of the DA algorithm. For the states, we specify that the voltage is within a plausible physiological range based on prior knowledge of the system and the variance in the observations. The gating variables are restricted to their dynamic range between 0 and 1. As for the parameters, it is difficult to know how tight the boundaries should be. As a rule of thumb, if it is possible to parameterise the model in a systematic and symmetric way, it may be easier to construct meaningful bounds. Also, it is advisable to keep the parameters within a bounding box which prevents blow-up of the dynamics such as divisions by zero. The maximal conductances are positive valued, and the sign of the slope for the steady-state gating functions should dictate if they are activating (positive) or inactivating (negative).

Background knowledge of the passive properties of the system, such as the capacitance and reversal potentials, can be informed from isolating step protocols by the electrophysiologist or voltage-clamp data if that is available.

### Implementation

We have implemented 4D-Var in a framework with CasADi, (Andersson *et al.*, 2019), in MATLAB. The “cas” comes from “computer algebra system”, in which the implementation of mathematical expressions resembles that of any other symbolic toolbox, and the “AD” for algorithmic (automatic) differentiation. These expressions are then easily used for generating derivatives by breaking the expressions into a number of atomic operations with explicit chain rules, with natural extensions to vector and matrix-valued functions. CasADi data types are all sparse matrices, and low-level scalar expressions (SX type) are stored as directed acyclic graphs where their numerical evaluation is conducted using virtual machines. For nonlinear programming problems, matrix expressions (MX type) are constructed to form the structure of the nonlinear program e.g. the collocation expression. The low-level expressions e.g. the differential equations are built using SX type to create a hierarchy of functions for evaluation efficiency and memory management. CasADi will generate the gradient and Hessian information through AD which are then passed to the solver of choice. We elect to solve the optimization problem with IPOPT (Interior Point OPTimize) (Wächter & Biegler, 2006). The high-dimensional linear algebra calculations are done using the linear solver MUMPS (MULTifrontal Massively Parallel sparse direct Solver) which is readily distributed with CasADi and interfaced with IPOPT.

### Conductance-based model

An issue with the original version of the mouse SCN model (Sim & Forger, 2007; Belle *et al.*, 2009) is that the structure is asymmetric with huge ranges of parameter values, which creates complications when constructing our optimization problem. We aim to fit to current-clamp data of the *R. pumilio* using the same set of currents, but expressing their kinetics uniformly. Additionally, we separate the leak into sodium and potassium components to investigate the role each may play in altering the resting membrane potential of cells in day versus night, as was done in (Diekman *et al.*, 2013). Lastly, we will approximate the sodium activation as instantaneous, as has been done previously to reduce the dimensionality of the

SCN model (Sim & Forger, 2007). Conversely, we will allow the inactivation of sodium to have a wide range of permissible time constant values, as persistent sodium is known to play a role in maintaining the pace of firing (Harvey *et al.*, 2020). Thus, our sodium channel functionally plays the classical role of a transient sodium current in generating the upstroke of the action-potential, but also is possibly involved in governing certain sub-threshold properties. The full model is described by the following equations:

$$\begin{aligned}
 C \frac{dV}{dt} &= I_{app}(t) - I_{Na} - I_K - I_{Ca} - I_{L_{Na}} - I_{L_K} - I_H - I_A - I_{syn-E} - I_{syn-I} \\
 &= I_{app}(t) - g_{Na}m_{Na}^3h_{Na}(V - E_{Na}) - g_Kn^4(V - E_K) - g_{Ca}m_{Ca}h_{Ca}(V - E_{Ca}) - g_{L_{Na}}(V - E_{Na}) \\
 &\quad - g_{L_K}(V - E_K) - g_Hm_H(V - E_H) - g_Am_A^3h_A(V - E_K) \\
 &\quad - g_{syn-E}s(t)(V - E_{syn-E}) - g_{syn-I}s(t)(V - E_{syn-I}) \\
 \frac{dq}{dt} &= \frac{q_\infty(V) - q}{\tau_q(V)}, \quad q = \{m_i, h_i, n\} \\
 q_\infty(V) &= \frac{1}{2} + \frac{1}{2} \tanh\left(\frac{V - v_q}{d\tau_q}\right) \\
 \tau_q(V) &= \tau_{q0} + \tau_{q1} \left(1 - \tanh^2\left(\frac{V - v_q}{d\tau_q}\right)\right)
 \end{aligned}$$

where  $C$  is membrane capacitance,  $V$  is membrane potential,  $I_{app}(t)$  is the applied current,  $I$  are ionic currents,  $g$  are maximal conductances,  $E$  are reversal potentials, and  $q$  are gating variables with steady-state functions  $q_\infty$  and time constants  $\tau_q$ . The active conductance of a channel,  $G$ , is the product of its maximal conductance and gating variables, e.g.  $G_{Na} = m_{Na}^3h_{Na}$ . The  $g_A$  and  $\tau_{h_A}$  scaling factors used in Figures 6 and 7 are coefficients that multiply the maximal conductance parameter and time constant variable, respectively. The scaling factor for the ratio of potassium to sodium leak conductance used in Figures 7 and S4 is a coefficient that divides  $g_{L_{Na}}$  and multiplies  $g_{L_K}$ . We calculated the synaptic gating variable  $s(t)$  from voltage-clamp recordings of post-synaptic currents in *R. pumilio* SCN neurons with the cells held at -70 mV. The synaptic currents  $I_{syn-E}$  and  $I_{syn-I}$  were not used in the DA procedure, and were only included in the model simulations shown in Figure 7A-B. The  $I_H$  and  $I_A$  currents were only included in the DA procedure and model simulations shown in Figures 6B-C and 7.

### Downsampling

We utilized a downsampling strategy on the current-clamp data in order to facilitate the use of longer stretches of data without exceeding the computational limits on the size of the optimization problem that our computing resources can handle. We set a threshold of -20 mV for each action potential, and within a region of 30 ms on either side of when this threshold is hit, the full 25 kHz sampling is preserved. Outside of this window, the data used is downsampled by some factor. For the results presented here, we used a downsampling factor of 5 so that during the action potential the resolution is 25kHz and outside the time window of the action potential it is 5kHz. With this strategy, we can retain as many data points as possible during the action potential, which occurs on a much faster timescale than the membrane dynamics during the interspike interval and enables us to better fit the spike shape. We also used the full 25 kHz sampling for the 30 ms region immediately following the onset or offset of the depolarizing and hyperpolarizing pulses.

### Multiple observations

A novel component of our DA approach is the use of multiple observations to inform a unified model for each cell's electrophysiology. We are restricted through a computational and memory budget with regard to our implementation on the amount of data we can use for each estimation. In a sense, we have a series of variational sub-problems solved

simultaneously which are connected through mutually shared parameters. We use symmetric current-clamp protocols which start with spontaneous activity, followed by either a depolarizing or hyperpolarizing step for 1s, and a subsequent return to spontaneous activity. We use a period of a few hundred ms prior to two different hyperpolarizing steps so as to access leak channel information and transient inactivation profiles. We use two similar segments from the return from hyperpolarizing steps to inform de-inactivation and activation time scales from rest. We use similar data for two responses to depolarizing steps to characterize the firing profiles and understand the limiting behavior for high-amplitude depolarizing pulses, including regular firing, firing with adaptation, or silence. We bias the data with a large segment (1500 ms) of data during spontaneous activity to reproduce the hallmark spontaneous activity and spike shape in our estimated models. In the problem construction shown by Figure S1, 4.5 seconds of data in total are used for the assimilation, amounting to around 36,000 time points after incorporating our downsampling strategy.

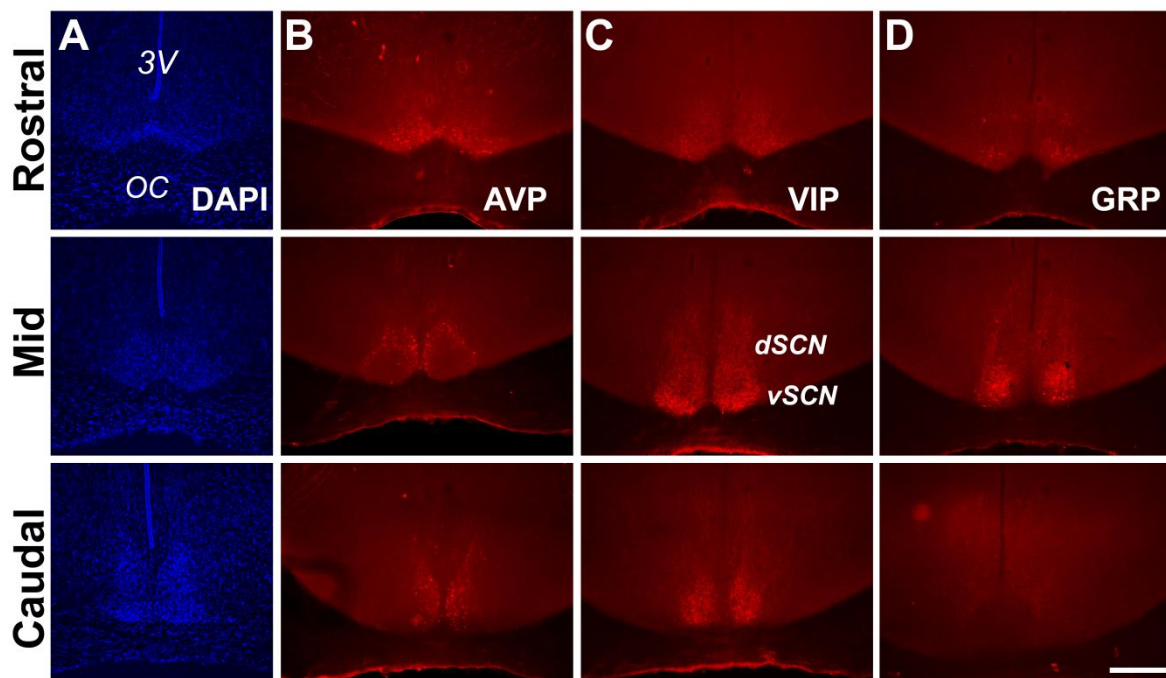
### Acknowledgements

We would like to thank the members of the University of Manchester Biological Services Facility for their excellent assistance in colony maintenance and husbandry. We also thank Profs Luckman and Andy Randall for allowing us access to their electrophysiology equipment.

This work was funded by a Biotechnology and Biological Sciences Research Council (BBSRC) Industrial Partnership Award with Signify (BB/P009182/1) to RJL, and by grants from the BBSRC to MDCB (BB/S01764X/1) and to TMB (B/N014901/1), and the Wellcome Trust (210684/Z/18/Z) to RJL. This material is based upon work supported by grants from the National Science Foundation (DMS 155237), the US Army Research Office (W911NF-16-1-0584), and the US-UK Fulbright Commission to COD. MJM and COD gratefully acknowledge the financial support of the EPSRC via grant EP/N014391/1.

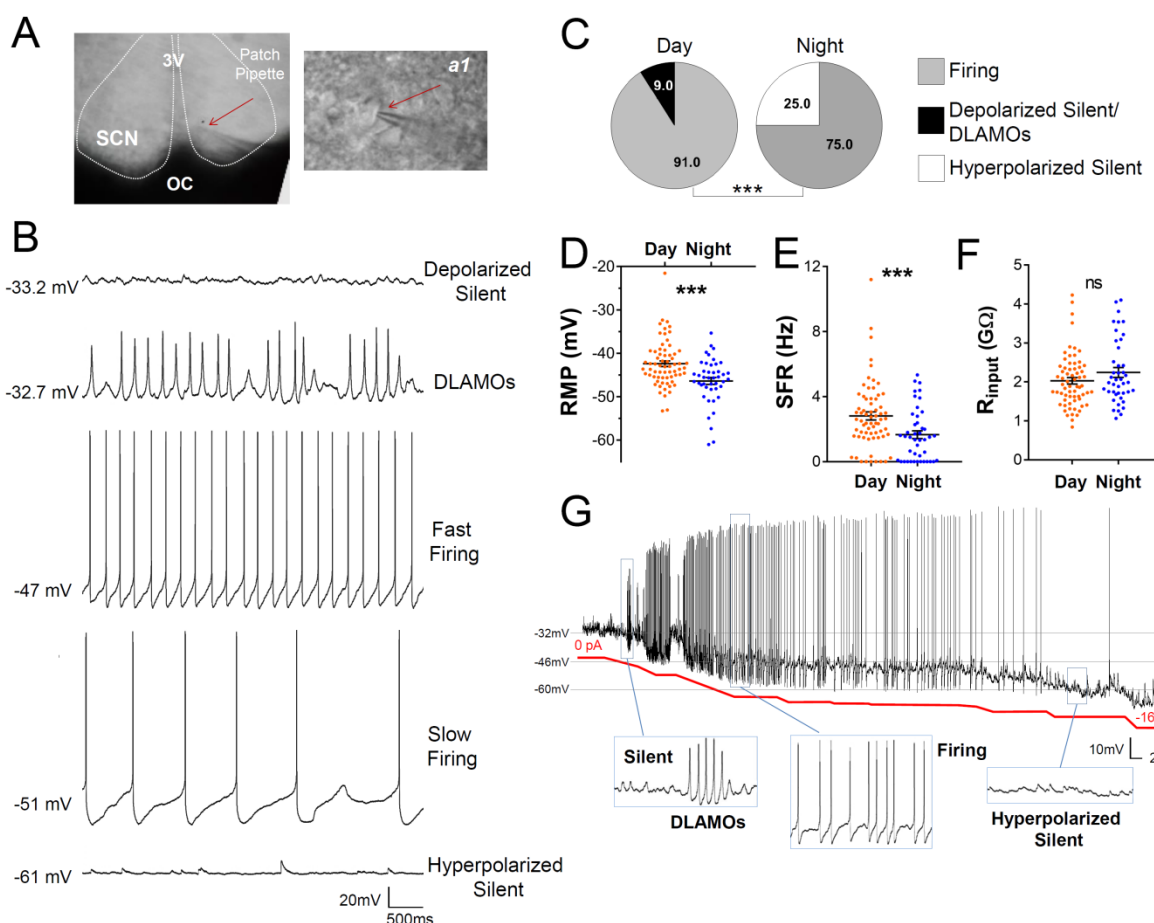
**Author contributions:** B.B.O, M.J.M, T.M.B, R.J.L, C.O.D and M.D.C.B conceived and designed research; B.B.O and M.D.C.B performed electrophysiology experiments; B.B.O performed data analysis; M.J.M and C.O.D performed mathematical modelling; B.B.O, M.J.M, T.M.B, R.J.L, C.O.D and M.D.C.B wrote the paper.

Figure 1



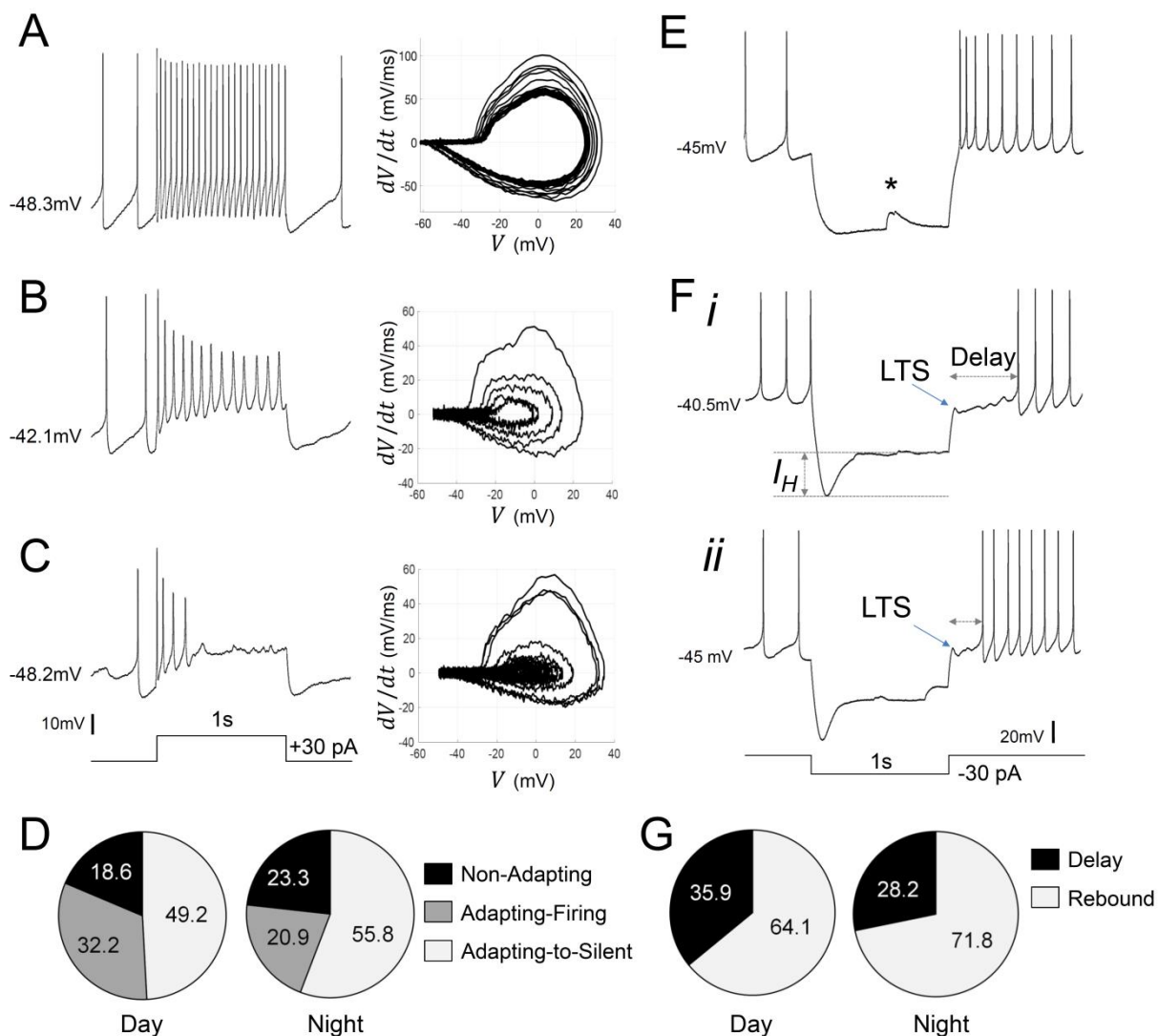
**Figure 1. Anatomy and neuropeptidergic organization of the *Rhabdomys pumilio* SCN.** (A) Coronal sections of the *R. pumilio* SCN taken across the rostro-caudal axis labelled with DAPI, and immunofluorescence for the main SCN neuropeptides: (B) Arginine-vasopressin (AVP), (C) Vasoactive intestinal peptide (VIP) and (D) Gastrin releasing peptide (GRP). 3V: third ventricle; OC: optic chiasm. dSCN: dorsal SCN, vSCN: ventral SCN. Labelling at the rostral level applies to mid and caudal aspects. Scale bar: 250  $\mu$ m.

**Figure 2**



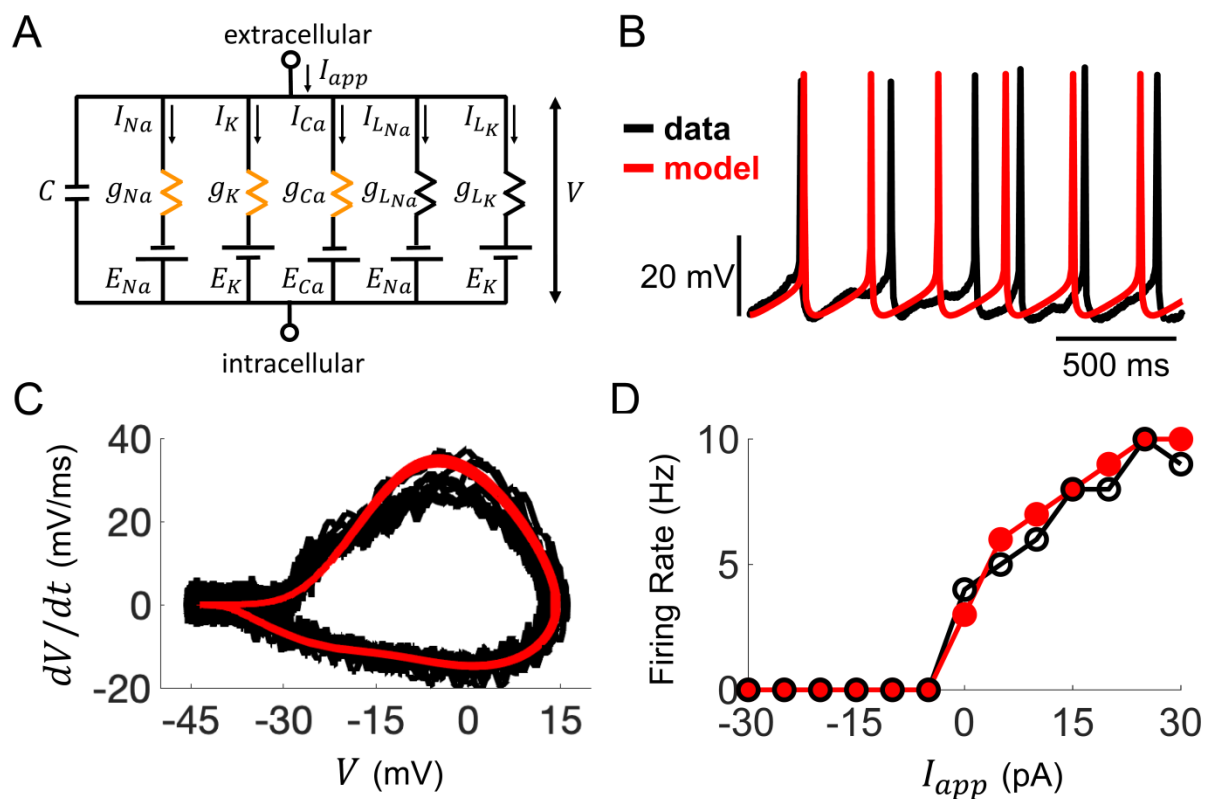
**Figure 2. Diurnal changes in the spontaneous electrical activity of *Rhabdomys pumilio* SCN neurons. (A)** Whole-cell patch clamp recording setup showing bright-field image of a SCN coronal brain slice. The SCN (delineated by white dotted lines) can be observed above the optic chiasm (OC), on either side of the third ventricle (3V). Patch pipette targeting a SCN neuron is indicated by the red arrow and magnified in inset (a1). **(B)** Representative current-clamp traces for each of the spontaneous excitability states recorded in *R. pumilio* SCN neurons (from top): highly depolarized-silent; depolarized low-amplitude membrane oscillations (DLAMOs); moderate resting membrane potential (RMP) with cells firing action potentials (APs) at high or low rate; and hyperpolarized-silent neurons. **(C)** Pie charts showing the percentages of SCN neurons in the different electrical states during the day and at night (\*\*p<0.001, Chi-Squared test). Mean RMP **(D)**, spontaneous firing rate (SFR) **(E)** and input resistance (R<sub>input</sub>) **(F)** of neurons recorded during the day (orange, n=67) and at night (blue, n=44). Data are expressed as mean  $\pm$  SEM with each dot representing an individual neuron. \*\*\*p  $\leq$  0.001, Mann-Whitney U-test. **(G)** Manual hyperpolarization of hyperexcited SCN neurons elicits a range of electrical states. Silent cell resting at highly depolarized state could be driven to display DLAMOs, fire APs, and become hyperpolarized-silent by injection of progressive steps of steady-state hyperpolarizing currents (red line).

**Figure 3**



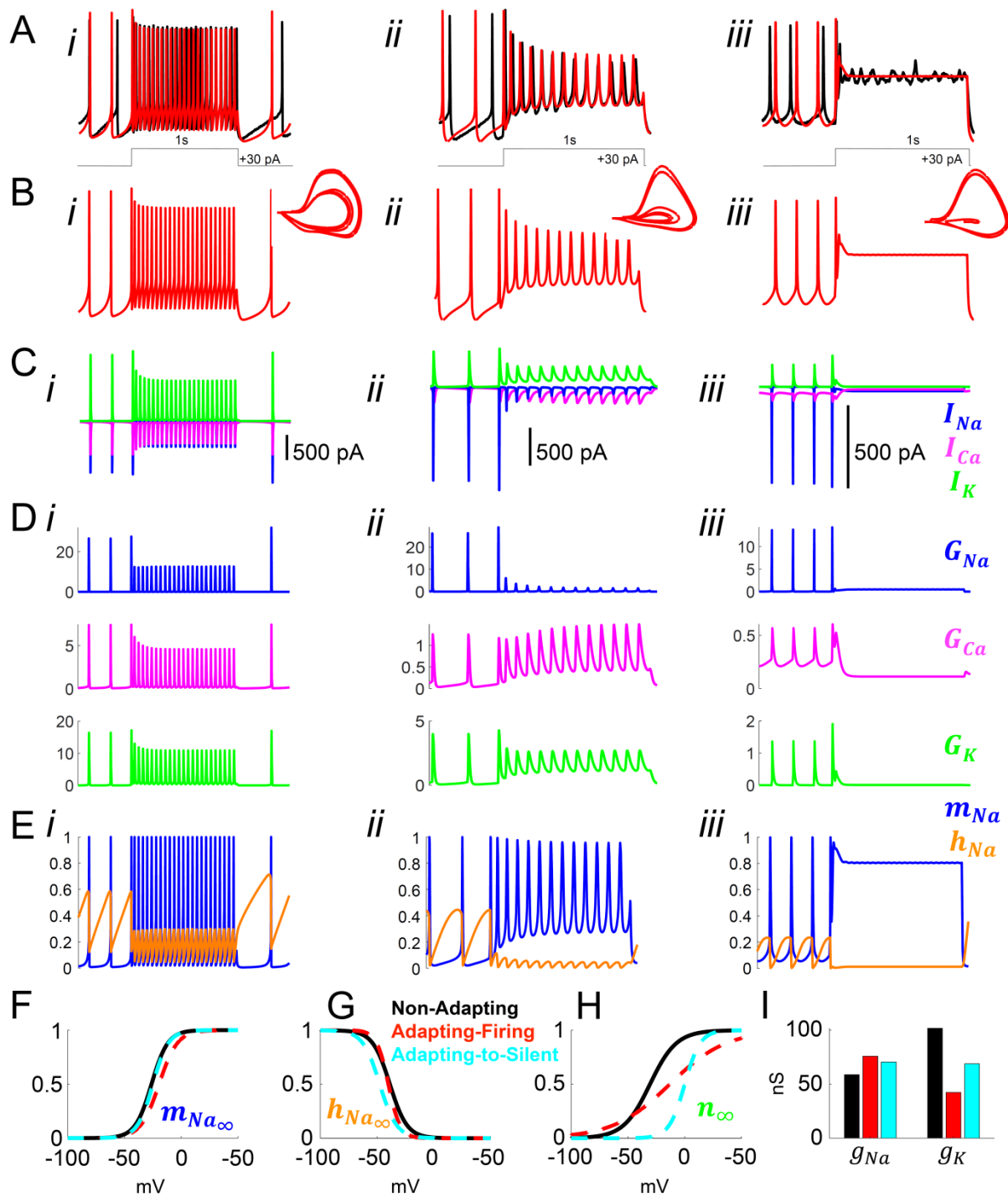
**Figure 3. Diverse responses to depolarizing and hyperpolarizing current pulses in *Rhabdomys pumilio* SCN neurons.** Representative current-clamp traces showing the different type of responses to a depolarizing pulse (1s, +30pA): **(A)** non-adapting; **(B)** adapting-firing; or **(C)** adapting-to-silent response. Phase-plot diagrams on the right of each panel (A, B, or C) show action potential (AP) velocity, trajectory and rate of frequency adaptation during the pulse for these neurons. **(D)** Pie charts showing the percentage of recorded neurons displaying each of these responses to depolarizing pulses during the day and at night. **(E-F)** Representative current-clamp traces showing the different type of responses to a 1s, -30pA hyperpolarizing pulse: **(E)** Type-A cells responded with a rebound spike upon termination of the pulse; **(F)** Type-B cells exhibited a rebound hyperpolarization which produced a delay-to-fire, following a LTS (*i*-*ii* long and short delay, respectively). **(G)** Pie charts showing the percentage of cells displaying a rebound spike or a delay-to-fire response during the day and at night. \* indicates a spontaneous synaptic input. LTS: low threshold spike.  $I_H$ : inward membrane rectification or depolarizing “sag”.

**Figure 4**



**Figure 4. Computational modelling of *Rhabdomys pumilio* SCN neurons.** **(A)** Schematic of conductance-based model for *R. pumilio* SCN neurons containing sodium ( $I_{Na}$ ), calcium ( $I_{Ca}$ ), potassium ( $I_K$ ), and leak ( $I_{LNa}$ ,  $I_{LK}$ ) currents. Orange resistors ( $g_{Na}$ ,  $g_{Ca}$ ,  $g_K$ ) indicate voltage-gated conductances, black resistors ( $g_{LK}$ ,  $g_{LNa}$ ) indicate passive leak conductances. **(B)** Voltage traces showing similarity in spontaneous firing of action potentials (APs) in the model (red) compared to a current-clamp recording from a *R. pumilio* SCN neuron (black). **(C)** Phase-plot of the derivative of voltage with respect to time ( $dV/dt$ ) as a function of voltage ( $V$ ) depicting the shape of APs in the model (red) and the current-clamp recording (black) during spontaneous firing. **(D)** Similarity in firing rate of the model (red) and current-clamp recordings (black) as a function of applied current ( $I_{app}$ ).

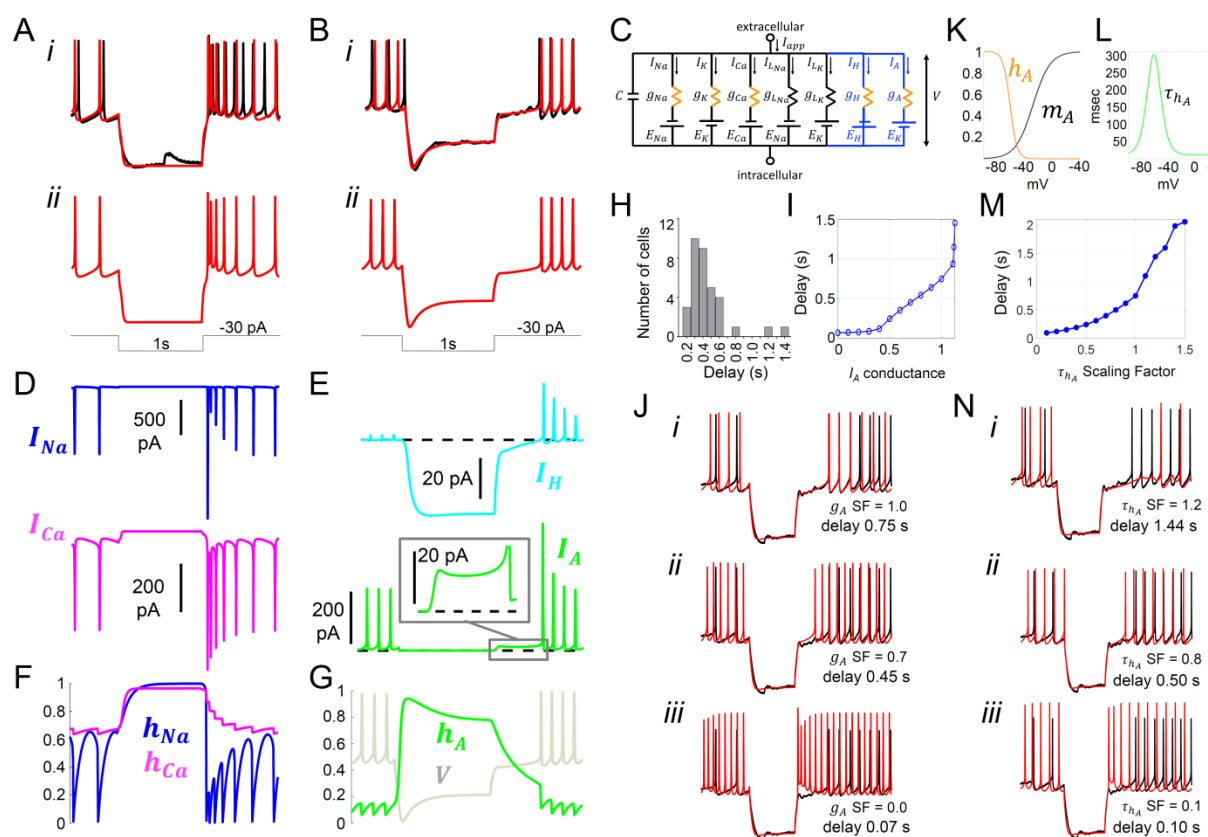
Figure 5



**Figure 5. Model simulation of the responses to depolarizing pulses in *Rhabdomys pumilio* SCN neurons and the underlying ionic mechanisms. (A-B)** Voltage traces of models (red) and current-clamp recordings (black) during depolarizing pulses (1s, +30 pA) showing non-adapting (*i*), adapting-firing (*ii*), and adapting-to-silent (*iii*) responses. **(C)** Ionic currents sodium ( $I_{Na}$ , blue), calcium ( $I_{Ca}$ , magenta), and potassium ( $I_K$ , green) in the models during the non-adapting (*i*), adapting-firing (*ii*), and adapting-silent (*iii*) responses. **(D)** Ionic conductances for sodium ( $G_{Na}$ , blue), calcium ( $G_{Ca}$ , magenta), and potassium ( $G_K$ , green) in

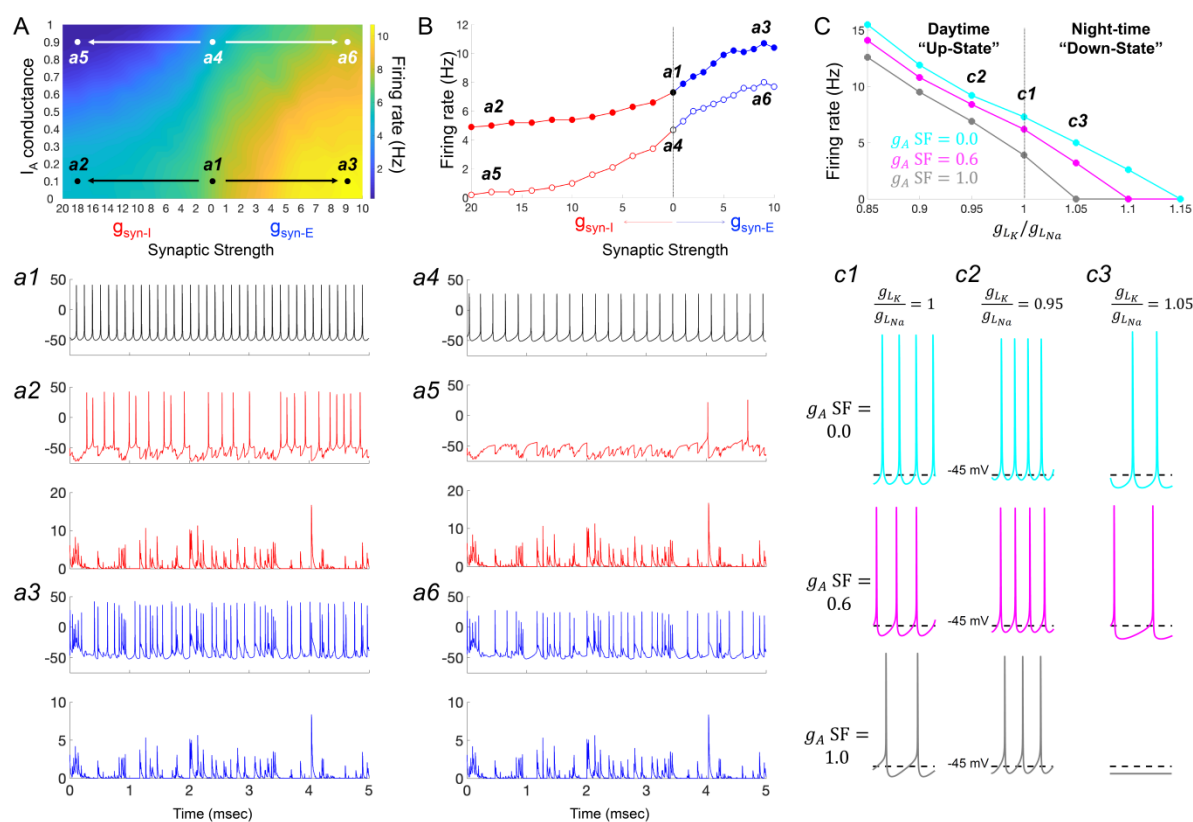
the models during the non-adapting (*i*), adapting-firing (*ii*), and adapting-silent (*iii*) responses. **(E)** Sodium activation ( $m_{Na}$ , blue) and inactivation ( $h_{Na}$ , orange) gating variables in the models during the non-adapting (*i*), adapting-firing (*ii*), and adapting-silent (*iii*) responses. Ions cannot pass through the channel if it is closed ( $m_{Na} = 0$ ) or inactivated ( $h_{Na} = 0$ ); maximal current flows when the channel is fully open ( $m_{Na} = 1$ ) and fully de-inactivated ( $h_{Na} = 1$ ). Steady-state gating variables as a function of voltage in the non-adapting (black), adapting-firing (red), and adapting-to-silent (cyan) models for **(F)** sodium activation ( $m_{Na\infty}$ ), **(G)** sodium inactivation ( $h_{Na\infty}$ ), and **(H)** potassium activation ( $n_\infty$ ). The flattening of the  $n_\infty$  curve in the adapting-firing model indicates that the channel is less activated at depolarized voltages than the non-adapting model (e.g. at -13 mV, the adapting-firing model is only half activated ( $n_\infty = 0.5$ ), whereas the non-adapting model is almost fully activated ( $n_\infty = 0.93$ )). **(I)** Maximal conductance parameters  $g_{Na}$  and  $g_K$  in the non-adapting (black), adapting-firing (red), and adapting-to-silent (cyan) models. Notice that the maximal potassium conductance parameter is much smaller in the adapting-firing model ( $g_K = 43$  nS) than in the non-adapting model ( $g_K = 102$  nS).

Figure 6



**Figure 6. Model simulation of the responses to hyperpolarizing pulses in *Rhabdomys pumilio* SCN neurons and the underlying ionic mechanisms.** (A-B) Voltage traces of models (red) and current-clamp recordings (black) during hyperpolarizing pulses (1s, -30 pA) showing rebound spiking of Type-A neurons (A) and delay responses of Type-B cells (B). (C) Schematic of conductance-based model for Type-B *R. pumilio* SCN neurons showing the addition of transient potassium ( $I_A$ ) and hyperpolarization-activated ( $I_H$ ) currents (blue). (D) Ionic currents for sodium ( $I_{Na}$ , blue) and calcium ( $I_{Ca}$ , magenta) in the model during the Type-A neuronal rebound spiking response. (E) Ionic currents  $I_H$  (cyan) and  $I_A$  (green) in the model during the delay response of Type-B neurons. (F) Sodium ( $h_{Na}$ , blue) and calcium ( $h_{Ca}$ , magenta) inactivation gating variables in the model during the Type-A neuronal rebound spiking response. (G) Transient potassium ( $I_A$ ) inactivation gating variable ( $h_A$ , green) in the model during the delay response in Type-B neurons (voltage trace,  $V$ , is indicated in grey and is the same  $V$ -trace shown in B). (H) Histogram showing delay-to-fire latencies measured in Type-B cells. (I) Relationship between  $I_A$  conductance ( $g_A$  Scaling Factor) and delay-to-fire latencies in model of Type-B cells. (J) Data trace for a cell with a 0.75 s delay (black) overlaid with model voltage traces (red) with varied amounts of  $I_A$  conductance: (i) model of Type-B cell with  $g_A$  SF = 1 exhibiting a 0.75 s delay; (ii) Model from (i) with reduced  $I_A$  conductance ( $g_A$  SF = 0.7) exhibiting a reduced delay-to-fire latency; (iii) Model from (i) with no  $I_A$  current ( $g_A$  SF = 0), exhibiting rebound spiking, as in Type-A neurons.  $g_A$  SF:  $g_A$  Scaling Factor. (K-L) Gating variable functions for model  $I_A$  current: (K) steady-state activation ( $m_A$ , black), steady-state inactivation ( $h_A$ , orange), and (L) inactivation time constant ( $\tau_{h_A}$ , green). (M) Relationship between the time constant of  $I_A$  inactivation and delay-to-fire latencies in model of Type-B cells. (N) Model simulations for  $I_A$  inactivation time constant scaling factors of 1.2 (i), 0.8 (ii) and 0.1 (iii).  $\tau_{h_A}$  SF:  $\tau_{h_A}$  Scaling Factor

**Figure 7**



**Figure 7.  $I_A$  conductances act to amplify extrinsic and intrinsic suppressive signals in the *Rhabdomys pumilio* SCN. (A)** Heatmap showing the overall effects of inhibitory ( $g_{\text{syn-I}}$ , red) and excitatory ( $g_{\text{syn-E}}$ , blue) physiological GABAergic synaptic conductances on firing frequency with increasing  $I_A$  conductances in the model *R. pumilio* SCN neurons. **(a1-a3)** Examples of firing activity in model cell with low  $I_A$  conductance ( $g_A$  SF = 0.1) and absence of GABAergic synaptic conductance (**a1**,  $g_{\text{syn-I}} = g_{\text{syn-E}} = 0$  nS), high suppressive GABAergic synaptic conductance (**a2**,  $g_{\text{syn-I}} = 18$  nS), or high excitatory GABAergic synaptic conductance (**a3**,  $g_{\text{syn-E}} = 9$ ). **(a4-a6)** Examples of firing activity in model *R. pumilio* SCN neurons with high  $I_A$  conductance ( $g_A$  SF = 0.9) and absence of GABAergic synaptic conductance (**a4**,  $g_{\text{syn-I}} = 0$  nS), high suppressive GABAergic synaptic conductance (**a5**,  $g_{\text{syn-I}} = 18$  nS), or high excitatory GABAergic synaptic conductance (**a6**,  $g_{\text{syn-E}} = 9$ ). **(B)** Firing rate as a function of inhibitory ( $g_{\text{syn-I}}$ , red) and excitatory ( $g_{\text{syn-E}}$ , blue) GABAergic synaptic conductances of different strength. Open and filled dots correspond to model cell with high (0.9) or low (0.1)  $I_A$  conductance ( $g_A$  SF), respectively. **(C)** Overall effect of intrinsic excitability states (scaling factor for the ratio of potassium leak current ( $g_{L_K}$ ) to sodium leak current ( $g_{L_Na}$ ) from 0.85 to 1.15) on firing frequency with increasing  $I_A$  conductances in the model cell ( $g_A$  SF = 0 (cyan), 0.6 (pink) and 1.0 (grey)).  $g_{L_K}/g_{L_Na}$  SF less than 1 corresponds to a daytime “up-state”, and a SF greater than 1 to a night-time “down-state”. **(c1)** Effect of  $I_A$  ( $g_A$  = 0, 0.6 and 1.0) on firing rate with nominal potassium/sodium leak current ratio ( $g_{L_K}/g_{L_Na}$  SF = 1). **(c2)** Effect of  $I_A$  ( $g_A$  SF = 0, 0.6 and 1.0) on firing rate with reduced potassium/sodium leak current ratio ( $g_{L_K}/g_{L_Na}$  SF = 0.95), representing daytime up-state. **(c3)** Effect of  $I_A$  ( $g_A$  SF = 0, 0.6 and 1.0) on firing rate with elevated potassium/sodium leak current ratio ( $g_{L_K}/g_{L_Na}$  SF = 1.05), representing night-time down-state. Notice that  $I_A$  amplifies the suppressive action of the low intrinsic excitability state (during down-state). SF: scaling factor.

**Figure S1**

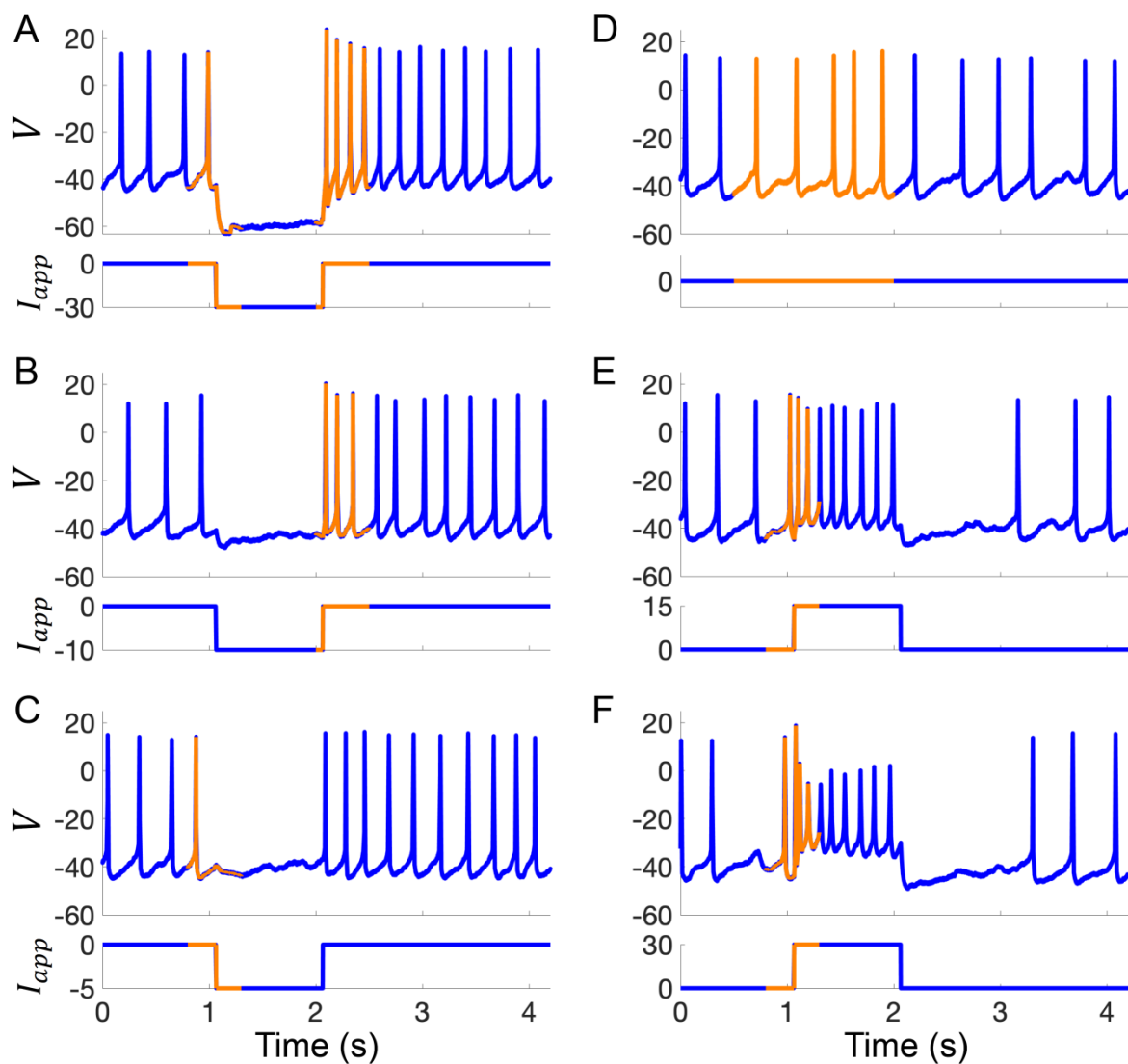


**Figure S1. Example current-clamp traces used in data assimilation algorithm for building computational models of *Rhabdomys pumilio* SCN neurons. (A-F)** Current-clamp recordings (blue) with the portion of the voltage trace used by the data assimilation algorithm (orange) to fit the model of rebound spiking in Type-A neuron shown in Figs. 4, 6A, and S2. **(A-C)** Hyperpolarizing current pulses. **(D)** Spontaneous activity. **(E-F)** Depolarizing current pulses.

Figure S2

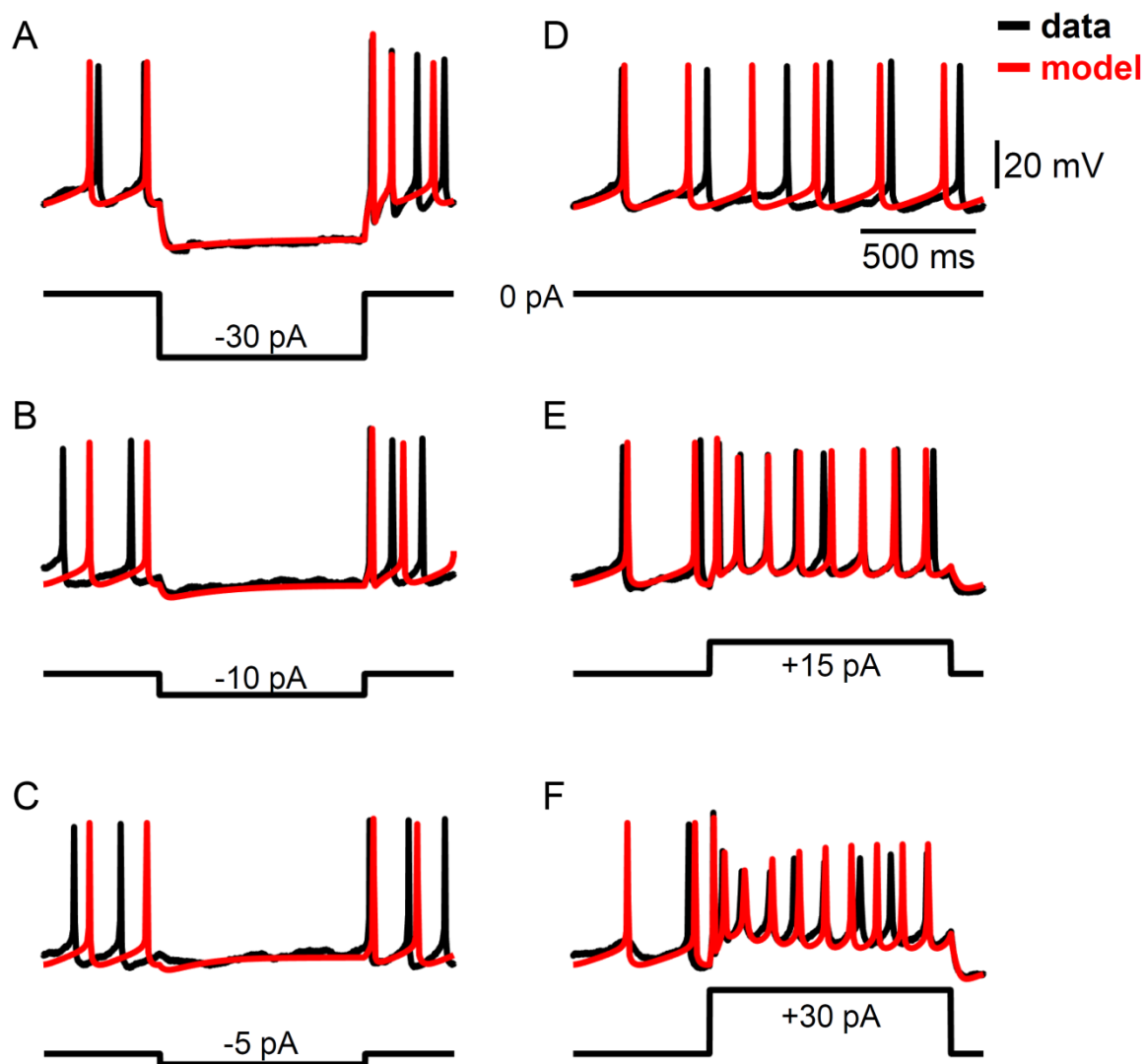
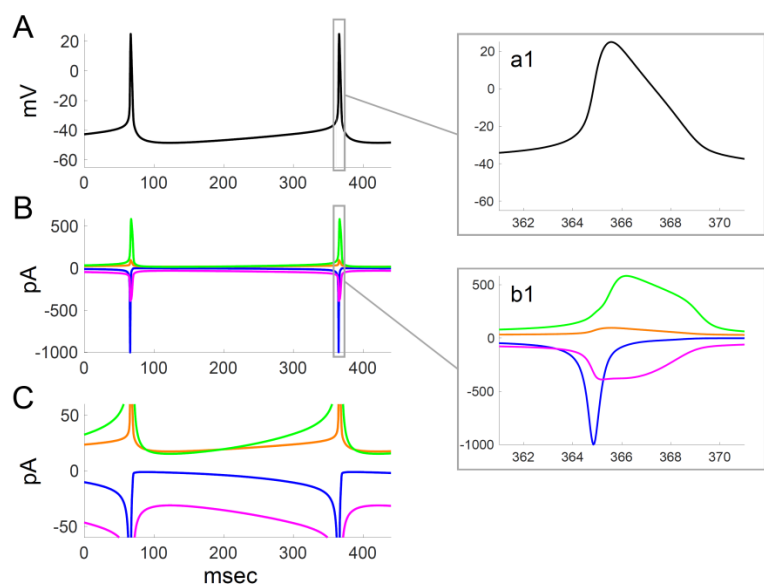


**Figure S2. Example voltage traces for a computational model of *Rhabdomys pumilio* SCN neurons fit using a data assimilation algorithm. (A-F)** Current-clamp recordings (black) and simulated voltage traces (red) from the model of rebound spiking in Type-A neurons shown in Figs. 4 and 6A using the portions of the data shown in Fig. S1. **(A-C)** Hyperpolarizing current pulses. **(D)** Spontaneous activity. **(E-F)** Depolarizing current pulses.

### Figure S3

#### Model of *Rhabdomys pumilio* SCN neurons



#### Model of mouse SCN neurons

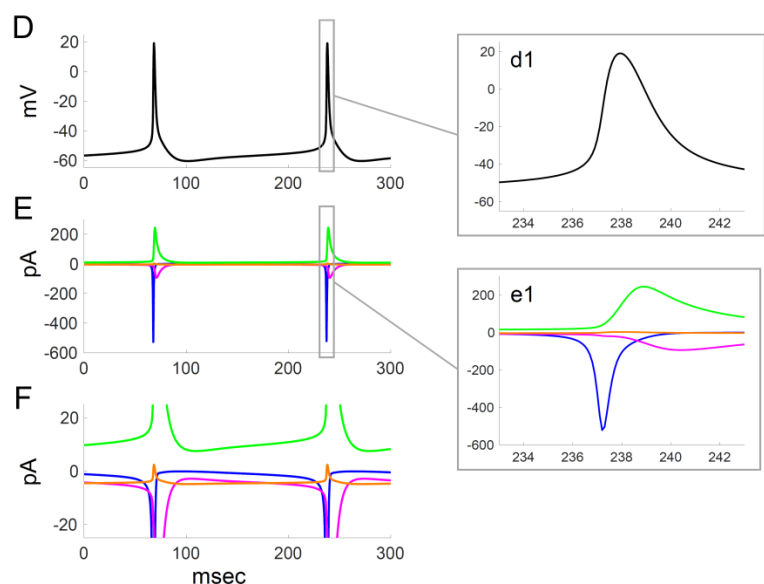


**Figure S3. Ionic currents underlying action potential generation in computational models of *Rhabdomys pumilio* and mouse SCN neurons.** **(A)** Voltage trace showing spontaneous firing in model of *R. pumilio* SCN neurons. **(a1)** Magnified view of second AP shown in (A). **(B)** Sodium ( $I_{Na}$ , blue), calcium ( $I_{Ca}$ , magenta), potassium ( $I_K$ , green), and leak ( $I_{LK} + I_{LNa}$ , orange) currents during the voltage trace shown in (A). **(b1)** Magnified view of currents during second AP shown in (A). **(C)** Same as (B), with y-axis scaled to emphasise the currents flowing during the interspike interval. **(D)** Voltage trace showing spontaneous firing in model of mouse SCN neurons. **(d1)** Magnified view of second AP shown in (D). **(E)** Sodium ( $I_{Na}$ , blue), calcium ( $I_{Ca}$ , magenta), potassium ( $I_K$ , green), and leak ( $I_{LK} + I_{LNa}$ , orange) currents during the voltage trace shown in (D). **(e1)** Magnified view of currents during second AP shown in (D). **(F)** Same as (E), with y-axis scaled to emphasise the currents flowing during the interspike interval.

**Figure S4**

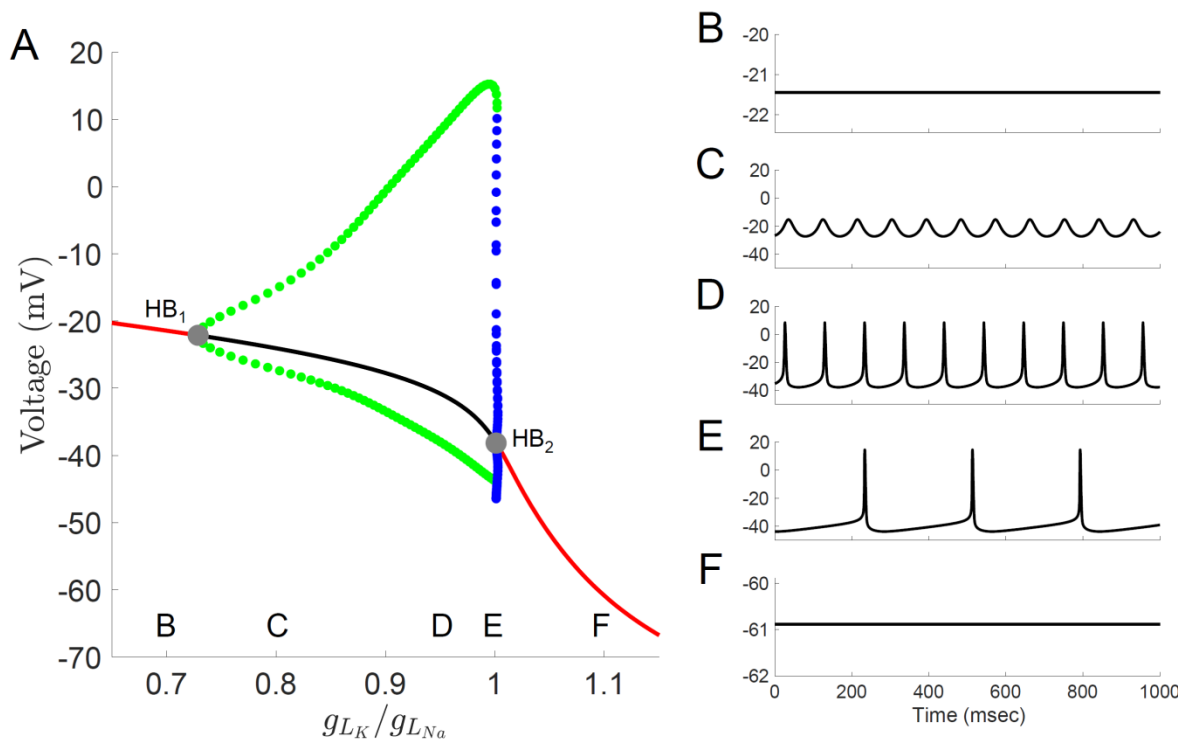


**Figure S4. Bifurcation diagram for a computational model of *Rhabdomys pumilio* SCN neurons. (A)** Voltage at steady-states and maximum/minimum voltage of oscillations for the model of rebound spiking in the Type-A neuron shown in Figs. 4, 6A, and S1-S3 with ratio of potassium leak current ( $g_{L_K}$ ) to sodium leak current ( $g_{L_{Na}}$ ) as the bifurcation parameter showing stable steady-states (black), unstable steady-states (red), stable periodic orbits (blue), and unstable periodic orbits (green). Stable periodic orbits correspond to spiking or DLAMOs. Transition from depolarized rest state to DLAMOs occurs through a supercritical Hopf bifurcation (grey dot  $HB_1$ ) and transition from spiking to hyperpolarized rest state occurs through a subcritical Hopf bifurcation (grey dot  $HB_2$ ). Model voltage traces showing each of the spontaneous excitability states: **(B)** highly depolarized-silent; **(C)** depolarized low-amplitude membrane oscillations (DLAMOs); moderate resting membrane potential (RMP) firing action potentials (APs) at high **(D)** or low rate **(E)**; and hyperpolarized-silent neurons **(F)**. According to the “bicycle model” proposed for the circadian regulation of electrical activity in mice and flies, a  $g_{L_K}/g_{L_{Na}}$  ratio scaling factor less than 1 corresponds to a daytime “up-state”, and a scaling factor greater than 1 to a night-time “down-state” (Flourakis *et al.*, 2015).

**Figure S5**

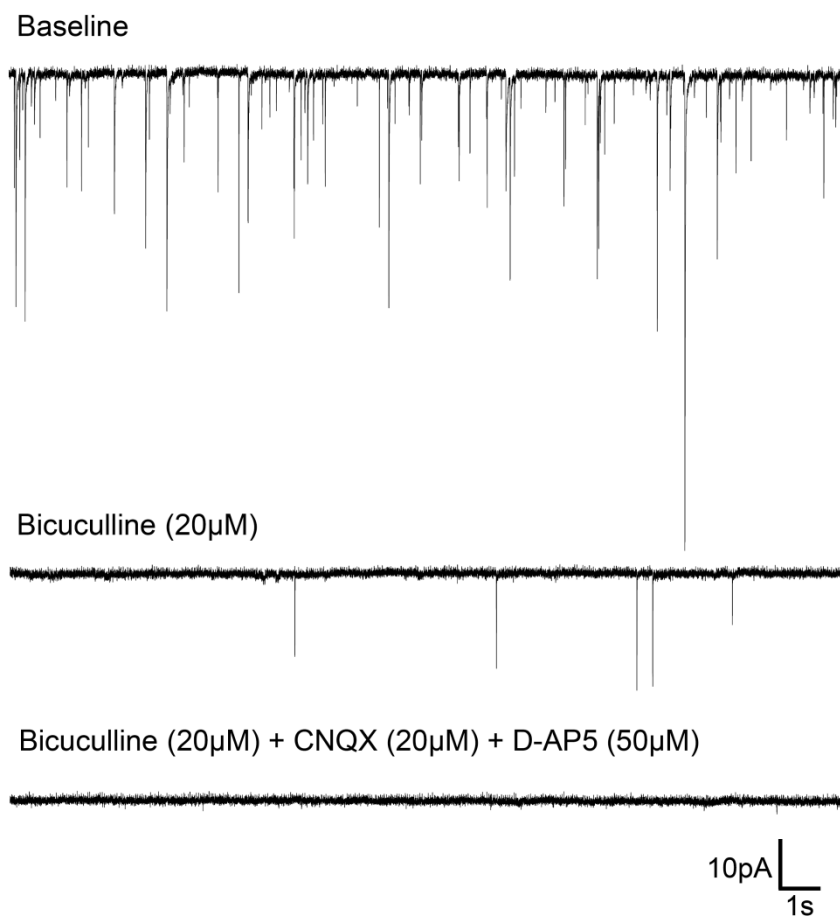


**Figure S5. Spontaneous synaptic events in *Rhabdomys pumilio* SCN neurons.**  
Representative trace from a SCN neuron (voltage-clamped at -70mV) showing post-synaptic currents (PSCs) under baseline conditions (top). Bath application of the GABA<sub>A</sub> receptor blocker, Bicuculline (20  $\mu$ M), abolished most synaptic events (middle trace); all PSCs were blocked under the presence of Bicuculline (20 $\mu$ M) and specific glutamatergic receptor antagonists, CNQX (20 $\mu$ M) and D-AP5 (50 $\mu$ M) (bottom trace).

**Table S1. Parameter values for the computational models of *Rhabdomys pumilio* SCN neurons.**

Symbol	Parameter	Units	Base Model (Fig. 4, S1-S4)	Non-Adapting (Fig. 5Ai)	Adapting-Firing (Fig. 5Aii)	Adapting-Silent (Fig. 5Aiii)	Type-A Rebound Spiking (Fig. 6A)	Type-B Delay (with IH) (Fig. 6B)	Type-B Delay (without IH) (Fig. 6i-N, 7)
C	whole-cell capacitance	pF	17.04	10.56	12.95	9.84	14.28	14.16	9.36
ENa	Na <sup>+</sup> reversal potential	mV	43.24	40.00	50.00	40.00	40.00	48.69	50
EK	K <sup>+</sup> reversal potential	mV	-100.00	-85.12	-100.00	-100.00	-80.00	-100.00	-100
Eca	Ca <sup>2+</sup> reversal potential	mV	123.89	130.00	130.00	130.00	130.00	130.00	87.69
EH	H-current reversal potential	mV	-	-	-	-	-	-40.00	-
gNa	INa maximal conductance	nS	88.58	58.81	75.92	70.50	90.70	53.27	500
gK	IK maximal conductance	nS	94.71	101.79	42.29	68.85	10.91	232.93	1.22
gCa	ICa maximal conductance	nS	5.13	13.08	4.17	3.74	6.02	7.86	2.01
gIH	IH maximal conductance	nS	-	-	-	-	-	5.34	-
gA	IA maximal conductance	nS	-	-	-	-	-	16.23	300
gLNa	ILNa maximal conductance	nS	0.44	0.16	0.17	0.22	0.13	0.00	0.02
gLK	ILK maximal conductance	nS	7.62	1.19	0.39	0.99	0.93	1.74	1.9
vm_Na	INa half-activation	mV	-24.78	-26.18	-19.53	-24.94	-21.07	-23.61	-19.11
dvm_Na	INa activation slope	mV	17.63	14.47	16.24	13.78	22.61	18.72	25.27
vh_Na	INa half-inactivation	mV	-44.46	-38.75	-40.04	-47.67	-39.49	-32.87	-58.18
dvh_Na	INa inactivation slope	mV	-12.89	-15.24	-10.35	-15.03	-14.30	-10.10	-19.16
th0_Na	INa inactivation time constant baseline	msec	0.47	0.95	0.43	0.22	0.37	0.70	1.42
th1_Na	INa inactivation time constant baseline	msec	72.38	400.00	400.00	120.40	223.00	400.00	156.07
vht_Na	INa inactivation time constant half-inactivation	mV	-33.64	-69.63	-68.76	-37.73	-70.00	vh_Na	vh_Na
dvht_Na	INa inactivation time constant slope	mV	17.09	16.22	24.39	13.88	21.09	16.09	17.82
vn_K	IK half-activation	mV	-6.51	-30.62	-13.18	0.00	-45.23	0.00	-48.23
dvn_K	IK half-activation slope	mV	11.08	23.38	50.00	13.79	39.56	13.01	19.37
tn0_K	IK activation time constant baseline	msec	0.01	0.16	1.26	0.01	0.21	1.62	0.94
tn1_K	IK activation time constant baseline	msec	16.59	25.20	40.00	40.00	40.00	11.87	40
vnt_K	IK activation time constant half-activation	mV	-30.62	-24.31	-18.50	-52.33	-0.79	vn_K	vn_K
dvnt_K	IK activation time constant slope	mV	31.03	24.50	23.64	36.15	9.44	13.32	7.75
vm_Ca	ICa half-activation	mV	-40.00	0.00	0.00	0.00	-6.78	-15.32	-40
dvm_Ca	ICa half-activation slope	mV	50.00	26.19	23.79	36.36	27.23	32.05	50
tm0_Ca	ICa activation time constant baseline	msec	0.22	0.01	3.41	9.32	0.01	8.55	10
tm1_Ca	ICa activation time constant baseline	msec	3.11	5.66	17.63	0.01	40.00	0.01	3.82
vmt_Ca	ICa activation time constant half-activation	mV	-36.62	-40.72	-24.55	-70.00	-57.85	vm_Ca	vm_Ca
dvmt_Ca	ICa activation time constant slope	mV	10.66	13.92	12.85	5.00	5.00	50.00	50
vh_Ca	ICa half-inactivation	mV	-17.72	-18.32	0.00	-34.43	-19.20	-42.15	0
dvh_Ca	ICa half-inactivation slope	mV	-9.56	-50.00	-5.01	-17.49	-42.83	-34.07	-50
th0_Ca	ICa inactivation time constant baseline	msec	284.73	3.80	1.90	30.30	3.10	0.01	200
th1_Ca	ICa inactivation time constant baseline	msec	3000.00	400.00	400.00	74.50	1000.00	15.20	400
vht_Ca	ICa inactivation time constant half-activation	mV	-15.99	-57.20	-61.13	0.00	-36.25	vh_Ca	vh_Ca
dvht_Ca	ICa inactivation time constant slope	mV	6.99	21.10	32.22	5.00	22.14	33.89	31.2
vm_H	IH half-activation	mV	-	-	-	-	-	-80.00	-
dvm_H	IH half-activation slope	mV	-	-	-	-	-	-17.19	-
tm0_H	IH activation time constant baseline	msec	-	-	-	-	-	283.40	-
tm1_H	IH activation time constant baseline	msec	-	-	-	-	-	484.40	-
vmt_H	IH activation time constant half-activation	mV	-	-	-	-	-	vm_H	-
dvmt_H	IH activation time constant slope	mV	-	-	-	-	-	30.00	-
vm_A	IA half-activation	mV	-	-	-	-	-	-35.00	-28.54
dvm_A	IA activation slope	mV	-	-	-	-	-	25.00	25
vh_A	IA half-inactivation	mV	-	-	-	-	-	-55.00	-61.68
dvh_A	IA inactivation slope	mV	-	-	-	-	-	-25.00	-10
th0_A	IA inactivation time constant baseline	msec	-	-	-	-	-	1.00	11.6
th1_A	IA inactivation time constant baseline	msec	-	-	-	-	-	211.40	291.2
vht_A	IA inactivation time constant half-inactivation	mV	-	-	-	-	-	vh_A	vh_A
dvht_A	IA inactivation time constant slope	mV	-	-	-	-	-	23.62	14.05

## References

Abarbanel, H.D.I. (2013) *Predicting the Future. Completing Models of Observed Complex Systems.* Springer, New York, NY.

Abarbanel, H.D.I.C., D.R. ; Farsian, R. ; Kostuk, M. (2009) Dynamical State and Parameter Estimation. *SIAM J Appl Dyn Syst*, **8**, 1341-1381.

Abrahamson, E.E. & Moore, R.Y. (2001) Suprachiasmatic nucleus in the mouse: retinal innervation, intrinsic organization and efferent projections. *Brain Res*, **916**, 172-191.

Aghajanian, G.K. (1985) Modulation of a transient outward current in serotonergic neurones by alpha 1-adrenoceptors. *Nature*, **315**, 501-503.

Albers, H.E., Walton, J.C., Gamble, K.L., McNeill, J.K.t. & Hummer, D.L. (2017) The dynamics of GABA signaling: Revelations from the circadian pacemaker in the suprachiasmatic nucleus. *Front Neuroendocrinol*, **44**, 35-82.

Allen, C.N., Nitabach, M.N. & Colwell, C.S. (2017) Membrane Currents, Gene Expression, and Circadian Clocks. *Cold Spring Harb Perspect Biol*, **9**.

Alvado, L. & Allen, C.N. (2008) Tetraethylammonium (TEA) increases the inactivation time constant of the transient K<sup>+</sup> current in suprachiasmatic nucleus neurons. *Brain Res*, **1221**, 24-29.

Amarillo, Y., De Santiago-Castillo, J.A., Dougherty, K., Maffie, J., Kwon, E., Covarrubias, M. & Rudy, B. (2008) Ternary Kv4.2 channels recapitulate voltage-dependent inactivation kinetics of A-type K<sup>+</sup> channels in cerebellar granule neurons. *J Physiol*, **586**, 2093-2106.

Andersson, J.A.E., Gillis, J., Horn, G., Rawlings, J.B. & Diehl, M. (2019) CasADI: a software framework for nonlinear optimization and optimal control. *Mathematical Programming Computation*, **11**, 1-36.

Atkinson, S.E., Maywood, E.S., Chesham, J.E., Wozny, C., Colwell, C.S., Hastings, M.H. & Williams, S.R. (2011) Cyclic AMP signaling control of action potential firing rate and molecular circadian pacemaking in the suprachiasmatic nucleus. *J Biol Rhythms*, **26**, 210-220.

Bano-Otalora, B., Martial, F., Harding, C., Bechtold, D.A., Allen, A.E., Brown, T.M., Belle, M.D.C. & Lucas, R.J. (2020) Daytime light enhances the amplitude of circadian output in a diurnal mammal. *bioRxiv*, 2020.2006.2022.164194.

Baranauskas, G. (2007) Ionic channel function in action potential generation: current perspective. *Mol Neurobiol*, **35**, 129-150.

Belle, M.D., Diekman, C.O., Forger, D.B. & Piggins, H.D. (2009) Daily electrical silencing in the mammalian circadian clock. *Science*, **326**, 281-284.

Belle, M.D., Hughes, A.T., Bechtold, D.A., Cunningham, P., Pierucci, M., Burdakov, D. & Piggins, H.D. (2014) Acute suppressive and long-term phase modulation actions of orexin on the mammalian circadian clock. *J Neurosci*, **34**, 3607-3621.

Belle, M.D. & Piggins, H.D. (2017) Circadian regulation of mouse suprachiasmatic nuclei neuronal states shapes responses to orexin. *Eur J Neurosci*, **45**, 723-732.

Belle, M.D.C. & Diekman, C.O. (2018) Neuronal oscillations on an ultra-slow timescale: daily rhythms in electrical activity and gene expression in the mammalian master circadian clockwork. *Eur J Neurosci*, **48**, 2696-2717.

Bouskila, Y. & Dudek, F.E. (1995) A rapidly activating type of outward rectifier K<sup>+</sup> current and A-current in rat suprachiasmatic nucleus neurones. *J Physiol*, **488 ( Pt 2)**, 339-350.

Brookings, T., Goeritz, M.L. & Marder, E. (2014) Automatic parameter estimation of multicompartmental neuron models via minimization of trace error with control adjustment. *J Neurophysiol*, **112**, 2332-2348.

Burdakov, D., Alexopoulos, H., Vincent, A. & Ashcroft, F.M. (2004) Low-voltage-activated A-current controls the firing dynamics of mouse hypothalamic orexin neurons. *Eur J Neurosci*, **20**, 3281-3285.

Burdakov, D. & Ashcroft, F.M. (2002) Cholecystokinin tunes firing of an electrically distinct subset of arcuate nucleus neurons by activating A-Type potassium channels. *J Neurosci*, **22**, 6380-6387.

Collins, B., Pierre-Ferrer, S., Muheim, C., Lukacsovich, D., Cai, Y., Spinnler, A., Herrera, C.G., Wen, S., Winterer, J., Belle, M.D.C., Piggins, H.D., Hastings, M., Loudon, A., Yan, J., Foldy, C., Adamantidis, A. & Brown, S.A. (2020) Circadian VIPergic Neurons of the Suprachiasmatic Nuclei Sculpt the Sleep-Wake Cycle. *Neuron*, **108**, 486-499 e485.

Colwell, C.S. (2011) Linking neural activity and molecular oscillations in the SCN. *Nat Rev Neurosci*, **12**, 553-569.

Connor, J.A. & Stevens, C.F. (1971) Voltage clamp studies of a transient outward membrane current in gastropod neural somata. *J Physiol*, **213**, 21-30.

de Jeu, M., Hermes, M. & Pennartz, C. (1998) Circadian modulation of membrane properties in slices of rat suprachiasmatic nucleus. *Neuroreport*, **9**, 3725-3729.

Dewsbury, D.A. & Dawson, W.W. (1979) African four-striped grass mice (*Rhabdomys pumilio*), a diurnal-crepuscular muroid rodent, in the behavioral laboratory. *Behavior Research Methods & Instrumentation*, **11**, 329-333.

Diekman, C.O., Belle, M.D., Irwin, R.P., Allen, C.N., Piggins, H.D. & Forger, D.B. (2013) Causes and consequences of hyperexcitation in central clock neurons. *PLoS Comput Biol*, **9**, e1003196.

Fleidervish, I.A., Friedman, A. & Gutnick, M.J. (1996) Slow inactivation of  $\text{Na}^+$  current and slow cumulative spike adaptation in mouse and guinea-pig neocortical neurones in slices. *J Physiol*, **493 (Pt 1)**, 83-97.

Flourakis, M., Kula-Eversole, E., Hutchison, A.L., Han, T.H., Aranda, K., Moose, D.L., White, K.P., Dinner, A.R., Lear, B.C., Ren, D., Diekman, C.O., Raman, I.M. & Allada, R. (2015) A Conserved Bicycle Model for Circadian Clock Control of Membrane Excitability. *Cell*, **162**, 836-848.

Gamble, K.L., Kudo, T., Colwell, C.S. & McMahon, D.G. (2011) Gastrin-releasing peptide modulates fast delayed rectifier potassium current in Per1-expressing SCN neurons. *J Biol Rhythms*, **26**, 99-106.

Golowasch, J., Goldman, M.S., Abbott, L.F. & Marder, E. (2002) Failure of averaging in the construction of a conductance-based neuron model. *J Neurophysiol*, **87**, 1129-1131.

Granados-Fuentes, D., Hermanstyne, T.O., Carrasquillo, Y., Nerbonne, J.M. & Herzog, E.D. (2015) IA Channels Encoded by Kv1.4 and Kv4.2 Regulate Circadian Period of PER2 Expression in the Suprachiasmatic Nucleus. *J Biol Rhythms*, **30**, 396-407.

Granados-Fuentes, D., Norris, A.J., Carrasquillo, Y., Nerbonne, J.M. & Herzog, E.D. (2012) IA channels encoded by Kv1.4 and Kv4.2 regulate neuronal firing in the suprachiasmatic nucleus and circadian rhythms in locomotor activity. *J Neurosci*, **32**, 10045-10052.

Hanna, L., Walmsley, L., Pienaar, A., Howarth, M. & Brown, T.M. (2017) Geniculohypothalamic GABAergic projections gate suprachiasmatic nucleus responses to retinal input. *J Physiol*, **595**, 3621-3649.

Hannibal, J., Hundahl, C., Fahrenkrug, J., Rehfeld, J.F. & Friis-Hansen, L. (2010) Cholecystokinin (CCK)-expressing neurons in the suprachiasmatic nucleus: innervation, light responsiveness and entrainment in CCK-deficient mice. *Eur J Neurosci*, **32**, 1006-1017.

Harvey, J.R.M., Plante, A.E. & Meredith, A.L. (2020) Ion Channels Controlling Circadian Rhythms in Suprachiasmatic Nucleus Excitability. *Physiol Rev*, **100**, 1415-1454.

Hermanstyne, T.O., Granados-Fuentes, D., Mellor, R.L., Herzog, E.D. & Nerbonne, J.M. (2017) Acute Knockdown of Kv4.1 Regulates Repetitive Firing Rates and Clock Gene Expression in the Suprachiasmatic Nucleus and Daily Rhythms in Locomotor Behavior. *eNeuro*, **4**.

Holmqvist, M.H., Cao, J., Hernandez-Pineda, R., Jacobson, M.D., Carroll, K.I., Sung, M.A., Betty, M., Ge, P., Gilbride, K.J., Brown, M.E., Jurman, M.E., Lawson, D., Silos-Santiago, I., Xie, Y., Covarrubias, M., Rhodes, K.J., Distefano, P.S. & An, W.F. (2002) Elimination of fast inactivation in Kv4 A-type potassium channels by an auxiliary subunit domain. *Proc Natl Acad Sci U S A*, **99**, 1035-1040.

Huang, R.C., Peng, Y.W. & Yau, K.W. (1993) Zinc modulation of a transient potassium current and histochemical localization of the metal in neurons of the suprachiasmatic nucleus. *Proc Natl Acad Sci U S A*, **90**, 11806-11810.

Itri, J.N., Vosko, A.M., Schroeder, A., Dragich, J.M., Michel, S. & Colwell, C.S. (2010) Circadian regulation of a-type potassium currents in the suprachiasmatic nucleus. *J Neurophysiol*, **103**, 632-640.

Jackson, A.C., Yao, G.L. & Bean, B.P. (2004) Mechanism of spontaneous firing in dorsomedial suprachiasmatic nucleus neurons. *J Neurosci*, **24**, 7985-7998.

Jerng, H.H., Kunjilwar, K. & Pfaffinger, P.J. (2005) Multiprotein assembly of Kv4.2, KChIP3 and DPP10 produces ternary channel complexes with ISA-like properties. *J Physiol*, **568**, 767-788.

Jerng, H.H., Lauver, A.D. & Pfaffinger, P.J. (2007) DPP10 splice variants are localized in distinct neuronal populations and act to differentially regulate the inactivation properties of Kv4-based ion channels. *Mol Cell Neurosci*, **35**, 604-624.

Jerng, H.H. & Pfaffinger, P.J. (2014) Modulatory mechanisms and multiple functions of somatodendritic A-type K (+) channel auxiliary subunits. *Front Cell Neurosci*, **8**, 82.

Jerng, H.H., Qian, Y. & Pfaffinger, P.J. (2004) Modulation of Kv4.2 channel expression and gating by dipeptidyl peptidase 10 (DPP10). *Biophys J*, **87**, 2380-2396.

Jeyaraj, D., Haldar, S.M., Wan, X., McCauley, M.D., Ripperger, J.A., Hu, K., Lu, Y., Eapen, B.L., Sharma, N., Ficker, E., Cutler, M.J., Gulick, J., Sanbe, A., Robbins, J., Demolombe, S., Kondratov, R.V., Shea, S.A., Albrecht, U., Wehrens, X.H., Rosenbaum, D.S. & Jain, M.K. (2012) Circadian rhythms govern cardiac repolarization and arrhythmogenesis. *Nature*, **483**, 96-99.

Jung, H.Y., Mickus, T. & Spruston, N. (1997) Prolonged sodium channel inactivation contributes to dendritic action potential attenuation in hippocampal pyramidal neurons. *J Neurosci*, **17**, 6639-6646.

Khaliq, Z.M. & Bean, B.P. (2008) Dynamic, nonlinear feedback regulation of slow pacemaking by A-type potassium current in ventral tegmental area neurons. *J Neurosci*, **28**, 10905-10917.

Kimm, T., Khaliq, Z.M. & Bean, B.P. (2015) Differential Regulation of Action Potential Shape and Burst-Frequency Firing by BK and Kv2 Channels in Substantia Nigra Dopaminergic Neurons. *J Neurosci*, **35**, 16404-16417.

Ko, C.H. & Takahashi, J.S. (2006) Molecular components of the mammalian circadian clock. *Hum Mol Genet*, **15 Spec No 2**, R271-277.

Kuhlman, S.J. & McMahon, D.G. (2004) Rhythmic regulation of membrane potential and potassium current persists in SCN neurons in the absence of environmental input. *Eur J Neurosci*, **20**, 1113-1117.

Liss, B., Franz, O., Sewing, S., Bruns, R., Neuhoff, H. & Roeper, J. (2001) Tuning pacemaker frequency of individual dopaminergic neurons by Kv4.3L and KChip3.1 transcription. *EMBO J*, **20**, 5715-5724.

Maffie, J., Blenkinsop, T. & Rudy, B. (2009) A novel DPP6 isoform (DPP6-E) can account for differences between neuronal and reconstituted A-type K(+) channels. *Neurosci Lett*, **449**, 189-194.

Meliza, C.D., Kostuk, M., Huang, H., Nogaret, A., Margoliash, D. & Abarbanel, H.D. (2014) Estimating parameters and predicting membrane voltages with conductance-based neuron models. *Biol Cybern*, **108**, 495-516.

Moye, M.J. (2020) Data assimilation for conductance-based neuronal models. *Dissertations*, 1459.

Mure, L.S., Le, H.D., Benegiamo, G., Chang, M.W., Rios, L., Jillani, N., Ngotho, M., Kariuki, T., Dkhissi-Benyahya, O., Cooper, H.M. & Panda, S. (2018) Diurnal transcriptome atlas of a primate across major neural and peripheral tissues. *Science*, **359**.

Nadin, B.M. & Pfaffinger, P.J. (2010) Dipeptidyl peptidase-like protein 6 is required for normal electrophysiological properties of cerebellar granule cells. *J Neurosci*, **30**, 8551-8565.

Park, S.K.X., L. (2013) *Data Assimilation for Atmospheric, Oceanic and Hydrologic Applications (Vol. II)*. Springer-Verlag Berlin Heidelberg, Berlin, Heidelberg.

Patel, A.X., Murphy, N. & Burdakov, D. (2012) Tuning low-voltage-activated A-current for silent gain modulation. *Neural Comput*, **24**, 3181-3190.

Paul, J.R., DeWoskin, D., McMeekin, L.J., Cowell, R.M., Forger, D.B. & Gamble, K.L. (2016) Regulation of persistent sodium currents by glycogen synthase kinase 3 encodes daily rhythms of neuronal excitability. *Nat Commun*, **7**, 13470.

Pennartz, C.M., De Jeu, M.T., Geurtsen, A.M., Sluiter, A.A. & Hermes, M.L. (1998) Electrophysiological and morphological heterogeneity of neurons in slices of rat suprachiasmatic nucleus. *J Physiol*, **506 ( Pt 3)**, 775-793.

Reppert, S.M. & Weaver, D.R. (2002) Coordination of circadian timing in mammals. *Nature*, **418**, 935-941.

Ruby, N.F. & Heller, H.C. (1996) Temperature sensitivity of the suprachiasmatic nucleus of ground squirrels and rats in vitro. *J Biol Rhythms*, **11**, 126-136.

Rudy, B. (1988) Diversity and ubiquity of K channels. *Neuroscience*, **25**, 729-749.

Rush, M.E. & Rinzel, J. (1995) The potassium A-current, low firing rates and rebound excitation in Hodgkin-Huxley models. *Bull Math Biol*, **57**, 899-929.

Saito, Y. & Isa, T. (2000) Voltage-gated transient outward currents in neurons with different firing patterns in rat superior colliculus. *J Physiol*, **528 Pt 1**, 91-105.

Sato, T. & Kawamura, H. (1984) Circadian rhythms in multiple unit activity inside and outside the suprachiasmatic nucleus in the diurnal chipmunk (*Eutamias sibiricus*). *Neurosci Res*, **1**, 45-52.

Schoppa, N.E. & Westbrook, G.L. (1999) Regulation of synaptic timing in the olfactory bulb by an A-type potassium current. *Nat Neurosci*, **2**, 1106-1113.

Schumann, D.M., Cooper, H.M., Hofmeyr, M.D. & Bennett, N.C. (2005) Circadian rhythm of locomotor activity in the four-striped field mouse, *Rhabdomys pumilio*: a diurnal African rodent. *Physiol Behav*, **85**, 231-239.

Schwartz, W.J. (1991) SCN metabolic activity in vivo. In Klein, D.C.M., R.Y.; Reppert, S.M. (ed) *Suprachiasmatic Nucleus: The Mind's Clock*. Oxford University Press, New York, pp. 144-156.

Shibata, R., Nakahira, K., Shibasaki, K., Wakazono, Y., Imoto, K. & Ikenaka, K. (2000) A-type K<sup>+</sup> current mediated by the Kv4 channel regulates the generation of action potential in developing cerebellar granule cells. *J Neurosci*, **20**, 4145-4155.

Sim, C.K. & Forger, D.B. (2007) Modeling the electrophysiology of suprachiasmatic nucleus neurons. *J Biol Rhythms*, **22**, 445-453.

Smale, L. & Boverhof, J. (1999) The suprachiasmatic nucleus and intergeniculate leaflet of *Arvicanthis niloticus*, a diurnal murid rodent from East Africa. *J Comp Neurol*, **403**, 190-208.

Sonoda, T., Li, J.Y., Hayes, N.W., Chan, J.C., Okabe, Y., Belin, S., Nawabi, H. & Schmidt, T.M. (2020) A noncanonical inhibitory circuit dampens behavioral sensitivity to light. *Science*, **368**, 527-531.

Thomson, A.M. & West, D.C. (1990) Factors affecting slow regular firing in the suprachiasmatic nucleus in vitro. *J Biol Rhythms*, **5**, 59-75.

Timothy, J.W.S., Klas, N., Sanghani, H.R., Al-Mansouri, T., Hughes, A.T.L., Kirshenbaum, G.S., Brienza, V., Belle, M.D.C., Ralph, M.R., Clapcote, S.J. & Piggins, H.D. (2018) Circadian Disruptions in the Myshkin Mouse Model of Mania Are Independent of Deficits in Suprachiasmatic Molecular Clock Function. *Biol Psychiatry*, **84**, 827-837.

Toth, B.A., Kostuk, M., Meliza, C.D., Margoliash, D. & Abarbanel, H.D. (2011) Dynamical estimation of neuron and network properties I: variational methods. *Biol Cybern*, **105**, 217-237.

van Oosterhout, F., Lucassen, E.A., Houben, T., vanderLeest, H.T., Antle, M.C. & Meijer, J.H. (2012) Amplitude of the SCN clock enhanced by the behavioral activity rhythm. *PLoS One*, **7**, e39693.

Wächter, A. & Biegler, L.T. (2006) On the implementation of an interior-point filter line-search algorithm for large-scale nonlinear programming. *Mathematical Programming*, **106**, 25-57.

Wen, S., Ma, D., Zhao, M., Xie, L., Wu, Q., Gou, L., Zhu, C., Fan, Y., Wang, H. & Yan, J. (2020) Spatiotemporal single-cell analysis of gene expression in the mouse suprachiasmatic nucleus. *Nat Neurosci*, **23**, 456-467.

Yang, F., Feng, L., Zheng, F., Johnson, S.W., Du, J., Shen, L., Wu, C.P. & Lu, B. (2001) GDNF acutely modulates excitability and A-type K(+) channels in midbrain dopaminergic neurons. *Nat Neurosci*, **4**, 1071-1078.